



# Energy efficient double-pass photovoltaic/thermal air systems using a computational fluid dynamics multi-objective optimisation framework

Moustafa Al-Damook<sup>a, b, \*</sup>, Zinedine Khatir<sup>c</sup>, Mansour Al Qubeissi<sup>b</sup>, Darron Dixon-Hardy<sup>d</sup>, Peter J. Heggs<sup>d</sup>

<sup>a</sup> Renewable Energy Research Centre, University of Anbar, Al Anbar Province, Iraq

<sup>b</sup> School of Mechanical, Aerospace and Automotive Engineering, Faculty of Engineering, Environment and Computing, Coventry University, Coventry CV1 2JH, United Kingdom

<sup>c</sup> School of Engineering and the Built Environment, Faculty of Computing, Engineering and the Built Environment, Birmingham City University, Birmingham B4 7XG, United Kingdom

<sup>d</sup> School of Chemical and Process Engineering, Faculty of Engineering and Physical Sciences, University of Leeds, Leeds LS2 9JT, United Kingdom

## ARTICLE INFO

### Keywords:

Computational fluid dynamics  
Design optimisation  
Double-pass double-duct  
Heat transfer  
Photovoltaic  
Thermal management

## ABSTRACT

Photovoltaic systems have undergone substantial growth for the past twenty years and more than 75% of the solar irradiance is absorbed, but only a small amount of the captured solar energy (e.g. 7–24%) is transformed into electricity. The remaining energy can cause overheating and damage to adhesive seals, delamination and non-homogeneous temperatures. In this paper a three-step strategy is presented for the development of an energy efficient hybrid photovoltaic/thermal air system by the combination of experimentally validated computation fluid dynamics and optimal Latin hypercubes design of experiments. The combined thermo-hydraulic and electrical performances of five air flow configurations are examined after the selection of several design parameters. The parametric study reveals that the most promising configuration is co-current air flow through two channels above and below the photovoltaic cell. A multi-objective design optimisation process is undertaken for this configuration, where the system is represented by three design variables: the collector, the depths of the lower air flow and the upper air flow channels. A 50-point design of experiments is constructed within the design variables space using a permutation genetic algorithm. The multi-objective design optimisation methodology entails an accurate surrogate modelling to create Pareto curves which demonstrate clearly the compromises that may be taken between fan fluid and electric powers, and between the electric and thermal efficiencies. The design optimisation demonstrates how the design variables affect each of the four system performance parameters. The thermal and electric efficiencies are improved from 44.5% to 50.1% and from 10.0% to 10.5%, respectively.

## Nomenclature

$A$	area ( $\text{m}^2$ )
$c_p$	specific heat capacity ( $\text{J kg}^{-1} \text{K}^{-1}$ )
$G$	solar irradiance ( $\text{W m}^{-2}$ )
$k$	thermal conductivity ( $\text{W m}^{-1} \text{K}^{-1}$ )
$L$	collector length (m)
$L_{\text{ent}}$	entry length (m)
$\dot{M}$	mass flow rate ( $\text{kg s}^{-1}$ )
$P$	power (W)
$P_{\text{er}}$	perimeter (wetted perimeter) (m)
$q$	heat transfer rate (W)

$T$	temperature (K or $^{\circ}\text{C}$ )
$u$	velocity component in x-direction ( $\text{m s}^{-1}$ )
$\vec{V}$	total velocity vector ( $\text{m s}^{-1}$ )
$\dot{V}$	volumetric flow rate ( $\text{m}^3 \text{s}^{-1}$ )
$\bar{V}$	mean inlet velocity ( $\text{m s}^{-1}$ )
$v$	velocity component in y-direction ( $\text{m s}^{-1}$ )
$w$	velocity component in z-direction ( $\text{m s}^{-1}$ )
$W$	collector width (m)

## Greek symbols

$\alpha$	thermal diffusivity ( $\text{m}^2 \text{s}^{-1}$ )
$\beta$	temperature coefficient ( $\text{K}^{-1}$ )

\* Corresponding author at: Renewable Energy Research Centre, University of Anbar, Al Anbar Province, Iraq.

E-mail address: [moustafa.adil@uoanbar.edu.iq](mailto:moustafa.adil@uoanbar.edu.iq) (M. Al-Damook).

$\delta$	depth of flow (m)
$\varepsilon$	emissivity (–)
$\eta$	efficiency (–)
$\kappa$	pressure loss coefficients (used in Eq. (10))
$\mu$	dynamic viscosity ( $\text{kg m}^{-1} \text{s}^{-1}$ )
$\rho$	density ( $\text{kg m}^{-3}$ )
$\tau$	transmissivity (–)
$\nu$	kinematic viscosity ( $\text{m}^2 \text{s}^{-1}$ )
$\phi$	independent fluid property (variable) (–)

### Non-dimensional parameters

$C_f$	conversion (correction) factor (used in Eq. (1))
$F$	Fanning friction factor
$g^f$	geometry factor
$Pr$	Prandtl number, $c_p \mu / k$
$Re$	Reynolds number, $4\dot{M}_f / \mu P_{er}$
$r_i$	normalised distance

### Subscripts and superscripts

amb	ambient
$c$	cross-sectional, or characteristic value
comb	combined
cu	Copper
$D$	depth
$f$	Fluid
$fi$	inlet fluid
$fm$	mean fluid
$fo$	outlet fluid
$G$	glass
$h$	hydraulic
ref	reference value
$S$	solar or surface
$ted$	tedlar
$th$	thermal
$U$	useful heat gain

### Abbreviations

Al	aluminium
CFD	computational fluid dynamics
DOF	degrees of freedom
EVA	ethylene-vinyl acetate
MEQ	minimum element quality
NOE	number of elements
PV/T	photovoltaic/thermal
STC	standard conditions

## 1. Introduction

It is well known that PV panel efficiency declines when the photovoltaic module (PV) is subject to ambient conditions without active cooling. Teo et al. [1] report a 1.8 °C increase in temperature for every 100 W m<sup>-2</sup> can incur a penalty of PV electrical efficiency between 8 and 9%. Combined (or hybrid) photovoltaic and thermal collection (PV/T) systems are solar radiation collectors designed to produce electricity and heat simultaneously and offer the potential to solve the problem of reduced electrical efficiency by removing heat from the PV module and maintaining a more optimum temperature. The waste heat can be used for several applications, including space heating and solar drying.

The importance of cooling the PV panel increases when they are installed in areas where the ambient temperature causes the PV panel to exceed 25 °C. If temperatures significantly exceed this, it becomes more very important to provide cooling. Different design concepts have been demonstrated by several studies, which make for an interesting range of solutions, including different air flow patterns, glazed/unglazed panels, passive/active cooling, which all aim to achieve high PV module efficiencies [2–7]. One study found that even in an ambient temperature of 8 to 9 °C and a moderate solar irradiance value 750 W m<sup>-2</sup>, the average cell temperature was reduced from 52 °C to 18 °C, by cooling with cold water at 10 °C to 12 °C [2]. Once energy payback periods are considered, there are substantial improvements in annual energy output [1] proving that the efforts to cool the PV panel are very well worthwhile. An important trade-off to consider is whether to use air or water as the cooling fluid. PV/T air systems are usually used, because they have less weight and design requirements, and are more affordable. However, the use of water is more effective owing to its greater thermal physical properties - heat capacity, thermal conductivity and density compared to air [8–10].

Experimental methods, either in a laboratory or in-situ, are cumbersome to undertake, which makes numerical studies a very effective way to achieve a PV/T system optimisation in order to improve their performance even when taking into account the various assumptions made to simply their solutions. In recent years, various attempts have been made to optimise PV systems numerically. For example, in [11] a single channel PV/T is optimised mathematically using genetic algorithms (GAs). In [12] a non-linear programming optimisation is implemented to analyse a PV/T system. Also, a multi-objective design optimisation is developed in [13] by combining the semi-analytical Taguchi method with an analysis of variance (ANOVA) and a GA. In [14], the Taguchi method is used for a stand-alone PV system with a semi-analytical solution. Lately, Özakın and Kaya [15] have combined experimental analysis with the Taguchi method and ANNOVA to optimise an air-based PV/T one pass system. However, there is limited or no research literature on the optimisation of double pass PV/T air systems.

There is limited, or no, research on double-pass design optimisations of PV/T air systems, to the best of our knowledge. In this study, we aim to investigate the optimisation of such PV/T air systems in a comparative study, with emphasis on combined electrical and thermal efficiencies. A formal CFD-based multi-objective design optimisation framework is laid out, which combines surrogate modelling with a radial-based function approach. Following [16], a multi-objective GA (MOGA) technique is performed to generate a Pareto front and determine the influence of parameters affecting both the thermal and electrical efficiencies. The key design parameters are presented in Section 2. In Section 3, a performance evaluation is made for the thermal and electrical power domains of the PV/T system. Details of the CFD model, including input parameters and mesh independence check, are presented in Section 4. The parametric study and key findings are presented in Section 5. The results are summarised in Section 6.

## 2. Key design parameters

The impact of design parameters on the performance of PV/T air collectors is presented in this section. The examination of these parameters provides an understanding of how they influence the design and in turn, the performance of a PV/T system. Several parameters have been adopted and studied over the last two decades in order to enhance the electrical and thermal performance for PV/T systems such as the geometry and operational parameters. This section is focused on the relevant parameters of interest to this study and can be divided into four main groups, as follows:

- Geometry parameters, for example, duct length and depth of flow.

- Electrical parameters, such as short-circuit current and open-circuit voltage.
- Climate parameters such as ambient temperature ( $T_{amb}$ ) and solar irradiance ( $G$ ).
- Operational parameters such as mass flow rate.

In this study, the optimisation procedure is implemented to choose the most compatible dimensions within certain requirements. This design optimisation is based on multi-objectives to maximise both thermal and electrical efficiencies of PV/T air collector and minimise fan power required. Before proceeding to the formal optimisation, three steps are considered, as follows:

1. Defining the constant and variable parameters, considered in this examination.
2. Preliminary parametric studies are conducted for five proposed PV/T air flow arrangements (Configurations 1, 2, 3, 4 and 5) to identify the best performance for these conditions.
3. The best of these flow arrangements and configurations is used in the design optimisation process.

The selection of the ranges of geometrical parameters is based on literature values. However, when the parameters are unavailable in the literature, the selection is determined using a large range of design parameters but keeping it applicable to the real-world.

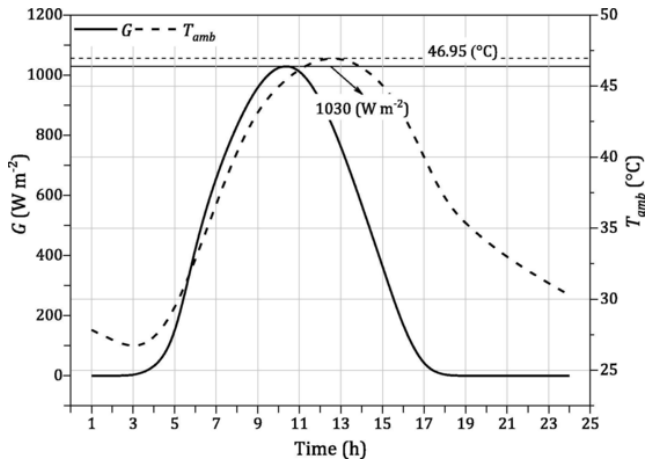


Fig. 1. Solar irradiance and ambient temperature versus time in a typical day on 1 July 2019.

**Table 1**  
Geometry design parameters used in the CFD design optimisation.

Symbol	Description	Values
$w$	Collector width	0.8 m [17–24]
$w_{\text{slice}}$	3D slice width	0.015 m
$t_{cu-U}$	Thickness of upper plate on the back surface	0.001 m [24]
$t_{cu-L}$	Thickness of the lower plate in lower channel flow	0.001 m [24]
$\delta_{D2}$	Upper depth flow	0.004–0.015 m [17,18,25–27]
$\delta_{D1}$	Lower depth flow	0.004–0.010 m [18,26,27]
$t_g$	Thickness of glass	4 mm [17,28,29]
$t_{UE}$	Equivalent thickness of glass and EVA	4.5 mm
$t_{LE}$	Equivalent thickness of Si, Tedlar and EVA	1.3 mm
$\epsilon_{cu}$	Emissivity of Copper (oxidized)	0.65 [28,29]
$\epsilon_g$	Average emissivity of glass	0.92 [28,29]
$L$	Collector length	0.6–1.3 m [19,20,22–24,26,27,30,31]

Table 1 lists the specifications of the range of geometrical parameters included the CFD design optimisation. For the sake of accuracy, the weather data was taken from [32] where the estimated weather parameters is carefully by validating the data with commonly cited set of data [33]. The cite is Photovoltaic Geographical Information System (PVGIS) which is accurate and widely used [34–36]. The proposed PV/T air systems are evaluated under two operating weather conditions in Iraq, Fallujah (33.34° N, 43.78° E). The first condition examines the PV/T air systems under hot weather, mainly at 45 °C, 1000 W m<sup>-2</sup>. This temperature is considered as the average of the hottest temperature, based on the local observation data in July 2019, Iraq, Fallujah, as shown in Fig. 1. The second condition evaluates the PV/T systems utilising precooled air (typically 25 °C [37–39]), where the exhaust air from the building is used as a coolant instead of using ambient air (45 °C) [40] (see Fig. 2).

In accordance with the ASHRAE Handbook [39], the exhaust air temperature is assumed to be in the range 22 °C–24 °C. This temperature range is estimated for the indoor design. However, for a building integrated PV/T system, the temperature can be higher, depending on different factors such as duct fitting and duct insulation type.

The material parameters are predetermined by the manufacturer and remain constant throughout this study. These parameters can be divided into collector body and PV module parts. In the collector body parts (air channel frame, glass cover and absorber plates), the selection of glass cover material type is based on durability, clarity and size of collector. In this study, 4 mm thickness glass cover is used. The design characteristics of the PV cells are determined by the photovoltaic reference efficiencies ( $\eta_{ref}$ ) which are dependent on the material type (mono-crystal silicon (mono c-Si), polycrystalline silicon (poly-Si) or non-silicon based film) [41–45]. In this study, poly-Si is used with a 0.83 packing factor value, 12.35 reference efficiency and 0.0041/°C temperature coefficient of power ( $\beta_{ref}$ ) [8,46,47]. The type of material also affects the optical properties of the PV module, such as thermal emissivity ( $\epsilon$ ). For example, the use of mono c-Si instead of poly-Si solar cells en-

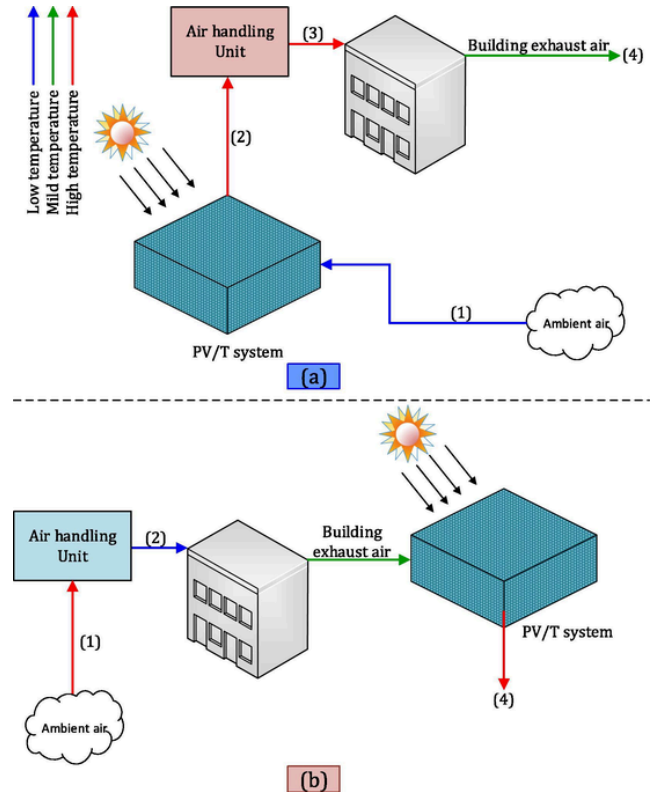


Fig. 2. Working principle of the studied BIPV/T system: in (a) winter mode and (b) summer mode [40].

hances the absorption coefficient and subsequently improves the thermal efficiency of the PV/T system [8,47]. However, the packing factor of poly-Si is greater than mono c-Si (i.e. more aperture area subjected to incident solar radiation). The poly-Si PV cells are also cheaper than mono c-Si and have a lower  $\beta_{\text{ref}}$  [48].

### 3. Thermal and electrical performance evaluation

Several parameters, such as pressure drop, effective thermal efficiency, fan power consumption and electrical power generation, are included in the thermo-hydraulic and electrical evaluation of the PV/T air collectors. The effective thermal efficiency ( $\eta_{th}$ ) is defined as the ratio of the heat benefit minus the equivalent fan power to the total incident solar radiation and given by the following expression:

$$\eta_{th} = [\dot{Q}_u - (P_{\text{fan}}/C_f)] / \dot{Q}_s \quad (1)$$

The PV/T heat benefit ( $\dot{Q}_u$ ) is equivalent to the increase in the enthalpy of the ( $\dot{M}_f \Delta h$ ) between the inlet and outlet air temperatures and is given by [49]:

$$\dot{Q}_u = \dot{M}_f \Delta h = \dot{M}_f C_p (T_{fo} - T_{fi}), \quad (2)$$

where  $\dot{M}_f$  is mass flowrate kg s<sup>-1</sup>, determined by:

$$\dot{M}_f = \rho \bar{V} A_c, \quad (3)$$

with  $\rho$  the density of air (kg m<sup>-3</sup>),  $\bar{V}$  the mean inlet velocity (m s<sup>-1</sup>) and  $A_c$  the channel ducting cross-section area (m<sup>2</sup>). The instantaneous fan power ( $P_{\text{fan}}$ ) is calculated as follows:

$$P_{\text{fan}} = \Delta p \dot{V}, \quad (4)$$

where the total pressure drop  $\Delta p$  (N m<sup>-2</sup>) in the flow arrangement at a volumetric flow of air  $\dot{V}$  (m<sup>3</sup> s<sup>-1</sup>). Two methods are used to evaluate the pressure drop: by a COMSOL software® built-in feature, and by the following empirical correlations:

$$\Delta p = \Delta p_f + \Delta p_{\text{dynamic}}, \quad (5)$$

$\Delta p_f$  is the pressure drop due to friction, expressed as:

$$\Delta p_f = \frac{\rho F \bar{V}^2 L}{2 D_h}, \quad (6)$$

$F$  is the Fanning friction factor for turbulent flow [17] and is calculated by Equation (7) and  $D_h$  is equivalent hydraulic diameter for inlet duct:

$$F = 0.079 \text{Re}^{-0.25} \quad 6000 < \text{Re} < 100000. \quad (7)$$

For laminar flow the Fanning friction factor is given by [65]:

$$F = \frac{g_f}{\text{Re}_{D_h}} \quad \{\text{Re} < 2550\}, \quad (8)$$

where  $g_f$  is the geometry factor and is taken to be 96.00 for parallel plates, because the ratios of the collector width  $w$  to depths of flow  $\delta_D$  are very large [50].

The dynamic losses ( $\Delta p_{\text{dynamic}}$ ) are caused by the flow effects at the channel entrance and exit. These are referred to as minor losses [51] and determined by:

$$\Delta p_{\text{dynamic}} = \left(\frac{1}{2}\right) \kappa_L \rho \bar{V}^2, \quad (9)$$

$$\kappa_L = \kappa_{\text{entrance}} + \kappa_{\text{exit}} + \kappa_{\text{bend}}. \quad (10)$$

The coefficients  $\kappa_{\text{entrance}}$  and  $\kappa_{\text{exit}}$  are set equal to 0.5 and 1.0 for the entrance and exit losses for single pass flow arrangements with  $\kappa_{\text{bend}}$  equal to zero. For a two pass arrangement  $\kappa_{\text{bend}}$  is taken equal to 2.2,

[52,53]. For the sake of completeness, the entrance and exit coefficients (minor losses) are added to the CFD model estimate of the pressure drop.

It is necessary to refer that the energy losses associated with the generation of the power consumed by the fan. Following [21,54–57], these losses are assumed as follows: the fan efficiency  $\eta_f = 0.65$ , the efficiency of the electric motor  $\eta_m = 0.88$ , the efficiency of electrical transmission from the power plant  $\eta_{tr} = 0.92$  and the thermal conversion efficiency of the power plant  $\eta_{thc} = 0.35$ . These coefficients can be shortened in a one named conversion correction factor ( $C_f$ ), which has a value of 0.18.

The total incident solar radiation ( $\dot{Q}_s$ ) projected on the absorber plate (W) is:

$$\dot{Q}_s = G A_s, \quad (11)$$

where  $G$  is the incident solar radiation (solar irradiance) and  $A_s$  is the surface area of the PV panel.

The electrical power generation in the PV module  $P_{PV}$  is estimated by [58–60]:

$$P_{PV} = I_m V_m = FF I_{sc} V_{oc} = -\frac{\tau_n \eta_{PV} A_s GPF}{V_{PV}}, \quad (12)$$

where  $I_m$  and  $V_m$  are the voltage and current at the maximum power point, respectively,  $FF$  is the Fill factor,  $I_{sc}$  is the short circuit current,  $V_{oc}$  is the open-circuit voltage [60],  $A_s$  is the total (aperture) surface area,  $V_{PV}$  is the total volume of PV cells and the packing factor is  $PF = 0.83$  (Poly-crystalline) [8,46,47].  $\tau_n$  is the transmissivity of the glass which changes based on the type and number of glass covers. The electrical efficiency of the PV module  $\eta_{PV}$  is calculated as follows [6,7,61,62]:

$$\eta_{PV} = \eta_{\text{ref}} (1 - \beta_{\text{ref}} (T_{mpv} - T_{\text{ref}})), \quad (13)$$

where  $\eta_{\text{ref}}$  is the reference electrical efficiency at standard conditions ( $G = 1000 \text{ W m}^{-2}$  and  $T_{\text{ref}} = 25^\circ \text{C}$ ) [63]. The temperature coefficient is assumed as  $\beta_{\text{ref}} = 0.0041 \text{ K}^{-1}$  for crystalline silicon modules [64]. The equivalent electrical efficiency of PV panel ( $\eta_{EPV}$ ) is estimated as:

$$\eta_{EPV} = \frac{\eta_{PV}}{C_{ff}}. \quad (14)$$

$C_{ff}$  is the conversion factor of the thermal power plant (in the range 0.29–0.4 [6,7,30,62,65,66]), and assumed equal to 0.36. The total combined PV/T collector (hybrid) efficiency ( $\eta_{\text{comb}}$ ) is obtained as follows [62,65]:

$$\eta_{\text{comb}} = \eta_{th} + \eta_{EPV}. \quad (15)$$

### 4. CFD model

The CFD mathematical representations of the configurations have been developed using COMSOL Multiphysics® v5.3a software (see Fig. 3). The thermal and electrical performances of the PV/T air systems are examined. Five different flow arrangements and configurations are investigated in this study: a standard PV module with no air flow (Configuration 1, see Fig. 3a), a standard PV module with air flow through a single duct below it (configuration 2, see Fig. 3b), a glazed single duct above a standard PV module and with air flow through a single duct below it (Configuration 3, see Fig. 3c), a standard PV module with parallel air flows through ducts above and below it (configuration 4, see Fig. 3d), a standard PV module with an airflow through the double-pass duct (Configuration 5, see Fig. 3e). The same depth of flow is used for the upper and lower channels (0.025 m) [17,18,25,29]. The collector original width (W) is 0.8 m, but the symmetry boundary condition is applied on two sides of the collector with a 3D slice width ( $W_{\text{slice}}$ ) of

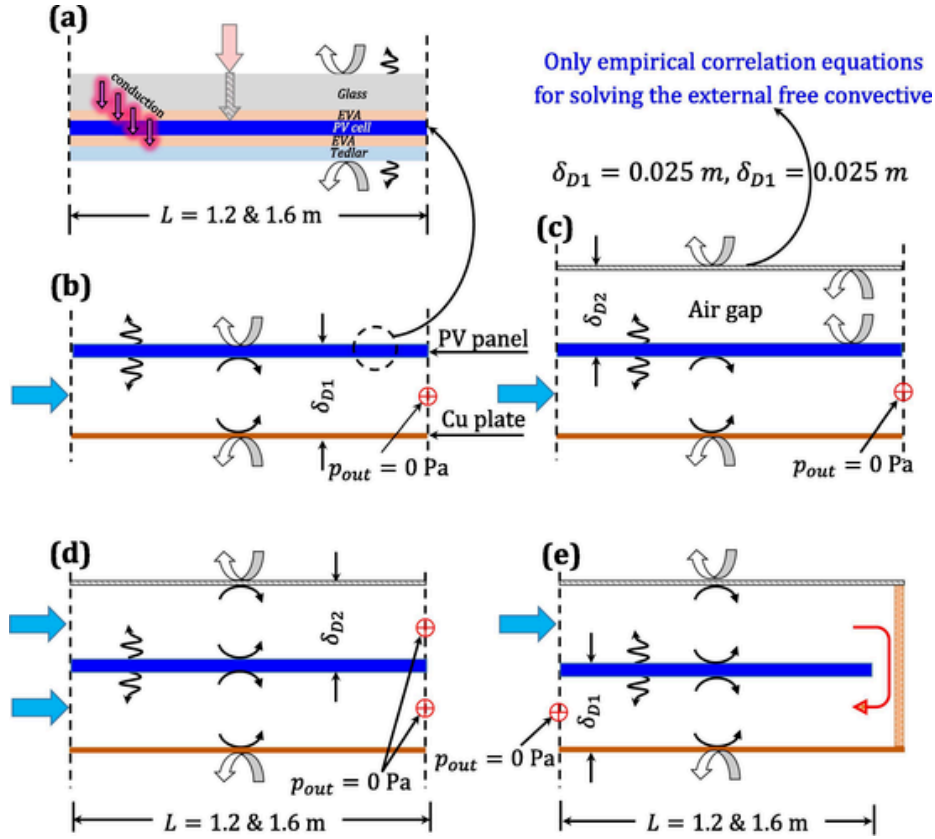


**Fig. 3.** Schematics of the various PV/T configurations, (a) Configuration 1, (b) Configuration 2, (c) Configuration 3, (d) Configuration 4 and (e) Configuration 5, along with indications of the flow of inlet air and flows of heat. These sketches are not made to scale.

0.015 m on the assumption that the collector is very wide, and any edge effects are negligible.

The full detail of the numerical simulation of all these configurations including the assumptions, boundary conditions can be found them in [32]. It can be found also the detail the governing equations for air velocity  $\vec{V}(x, y, z) = u, v, w$  and temperature  $T$  are based on the conservation of mass, momentum and energy. The software solves the Navier-Stokes equations for solving the kinetic and energy equations [67]. A three-dimensional conjugate heat transfer module is used to model the coupling between conduction heat transfer in a solid domain and convective heat transfer to the fluid at the solid/fluid interface [21]. However, the only empirical correlation equations are used to model the external convective heat transfer coefficient between the upper surface and the surrounding air (see Fig. 3c). Moreover, radiation model is mimic a realistic incident solar radiation. The surface-to-surface radiation model is used to simulate the thermal radiation exchange between the surfaces. The fluid is single-phase, laminar and weakly compressible. For weakly compressible flow  $\partial\rho/\partial p = 0$  and  $\partial\rho/\partial\phi \neq 0$ , where  $\phi$  are other independent variables, such as time. The range of Re number is between (510–2550) [68,69]. The ambient temperatures are assumed in the range 25 °C–45 °C. The inlet fluid temperature is taken equal to the ambient temperature ( $T_{fi} = T_{amb}$ ). The incident solar radiation is assumed as 1000 W m<sup>-2</sup>. The other assumptions and boundary conditions can be also seen in [32]. The entry length ( $L_{ent}$ ) is estimated as [70]:

$$L_{ent} = D_h [(0.631)^{1.6} + (0.0442\text{Re})^{1.6}]^{1/1.6}. \quad (16)$$

For the grid independence test, five parameters are considered in this investigation: solution time ( $t$  in sec), number of elements (NOE), degrees of freedom (DOF), physical random-access memory (RAM) in giga-bytes (GB), and minimum element quality (MEQ). The mesh is

made of square elements applied to the upper glass cover in XY-plane. The element size is varied from very coarse, less coarse and normal to highly refined, as shown in Table 2 (see Appendix B, Table B1 and Fig. B1 for further details). The same sizes and type of the element are used for the remaining parts of the system in the Z-direction. Increasing the number of elements has a small impact on the results. The same criteria are used to mesh the standard PV module, without the fluid domain.

In Table 2,  $Z_1$  is the edge size in the Z-direction in the upper and lower flow channels (in mm),  $Z_2$  is the number of divisions in the upper and lower flow channels in Z-direction, which is equal to  $(\delta_{D1}/Z_1)$  and

**Table 2**

Key features of the mesh structure for the grid independence test.

Trial No	Refinement step in X-Y direction	Bias	$Z_1(\text{mm})$	$Z_2$	$Z_3$
1	Very coarse	0	5	5	1
2	Less coarse	0	3.6	7	1
3	Coarse	0	2.27	11	2
3a	Coarse	8	0.83	30	2
3ab	Coarse	0	0.83	30	2
3abc	Coarse	0	0.71	35	2
3abcd	Coarse	8	0.71	35	2
4	Normal	0	1.56	16	2
5	Normal	0	1.25	20	2
6	Normal	0	1	25	2
7	Normal	5	1	25	2
7a	Normal	8	0.83	30	2
7ab	Normal	0	0.83	30	2
7abc	Normal	0	0.71	35	2
7abcd	Normal	8	0.71	35	2
8	Normal	8	1	25	2
9	Normal	12	1	25	2
10	Normal	17	1	25	2
11	Fine	0	0.84	30	2
12	Fine bias	8	0.84	30	2



$Z_3$  is the number of the divisions in PV and glass covers in Z-direction. A further examination is carried out to refine the mesh at the interfaces between the solid surface and the fluid flow to accurately estimate the field flow and temperature distribution.

The results reveal that this refinement has minor impacts on the mesh improvement, owing to the fact the laminar flow and the velocity gradient close to the wall is relatively small. The importance of latter mesh refinement, however, becomes more noticeable at  $Re \geq 2550$ , specially for  $\Delta p_f$ . This is because the entry length  $L_{ent}$  (m) is a function of the hydraulic diameter and Re number (see Equation (16)), which means that the velocity profile is not fully developed at the entrance, unlike the remaining duct length where the velocity profile is parabolic across the collector (see Fig. 4). This is also dependent on the flow arrangement. In order to compromise between the computational time and accuracy, case 3abcd in Table 2 is adopted in this study.

## 5. Preliminary parametric studies

A parametric study is made to establish the best performance of the PV/T air collector configurations and the best is subsequently analysed in the design optimisation process. The parametric study is carried out by understanding different operational, geometrical and weather parameters. A detailed comparison is made by the evaluation of their thermal, hydrodynamic and electrical parameters. Four of these designs (Configurations 2–5) are hybrid (PV/T) systems; while Configuration 1 is a standard PV system without active cooling. Configuration 1 is used as the benchmark in this comparison to highlight the impacts of the hybridisation. Accordingly, all configurations are named as ‘PV/T air systems’ for the sake of simplicity. Table 3 lists the parameters used in this study for the systems (Configurations 2–5). Configuration 1 is not a hybrid system (i.e., no duct flow); hence, is not included in this table.

This analysis is conducted using MATLAB® to account for the changes in operational parameters (mass flowrate and Reynolds number) and ambient temperatures, as presented in Table 3. Configurations 2, 3, 5 have one inlet, but Configuration 4 has two passes with the mass flowrates in the inlets of the upper and lower channels taken to be half of those of Configurations 2, 3 and 5. The pressure drop along the flow channel is plotted in Fig. 5 for different lengths, operational and weather conditions.

In Fig. 5, the pressure drop increases with increasing Re, length of collector and the ambient temperature, because there is a direct proportionality between the pressure drop, the length of collector and the mass flow rate. Also, increasing ambient/inlet temperature leads to an increase in the kinematic viscosity of inlet air velocity. In the same figure, Configurations 2 and 3 have similar pressure drops because they have a single flow of air passing underneath the PV module. The pressure drop is the lowest for Configuration 4 because of the two flow channels where the velocity is half of that in other designs (Configurations 2, 3 and 5); while the U-turn shape in Configuration 5 leads to extra pressure head losses in the U-flow region causing the maximum pressure loss, owing to the induced separation and swirling flows, because of the imbalance of centripetal forces [21]. The combined efficiencies (electrical plus thermal) evaluated by Equation (14) for the five arrangements are plotted against the range of Re numbers in Fig. 6.

The combined efficiencies (see Equation (15)) are evaluated for different Re numbers, weather conditions and lengths. The maximum combined efficiency occurs for arrangement 4 (curve in green in Fig. 6) at 25 °C because the lower ambient temperature gives a larger temperature difference between the inlet and outlet ducts, and also between the PV panel temperature and the local fluid one. To conclude, Configuration 4 has a maximum total efficiency with minimum fan power consumption (minimum pressure drop, see Fig. 5).

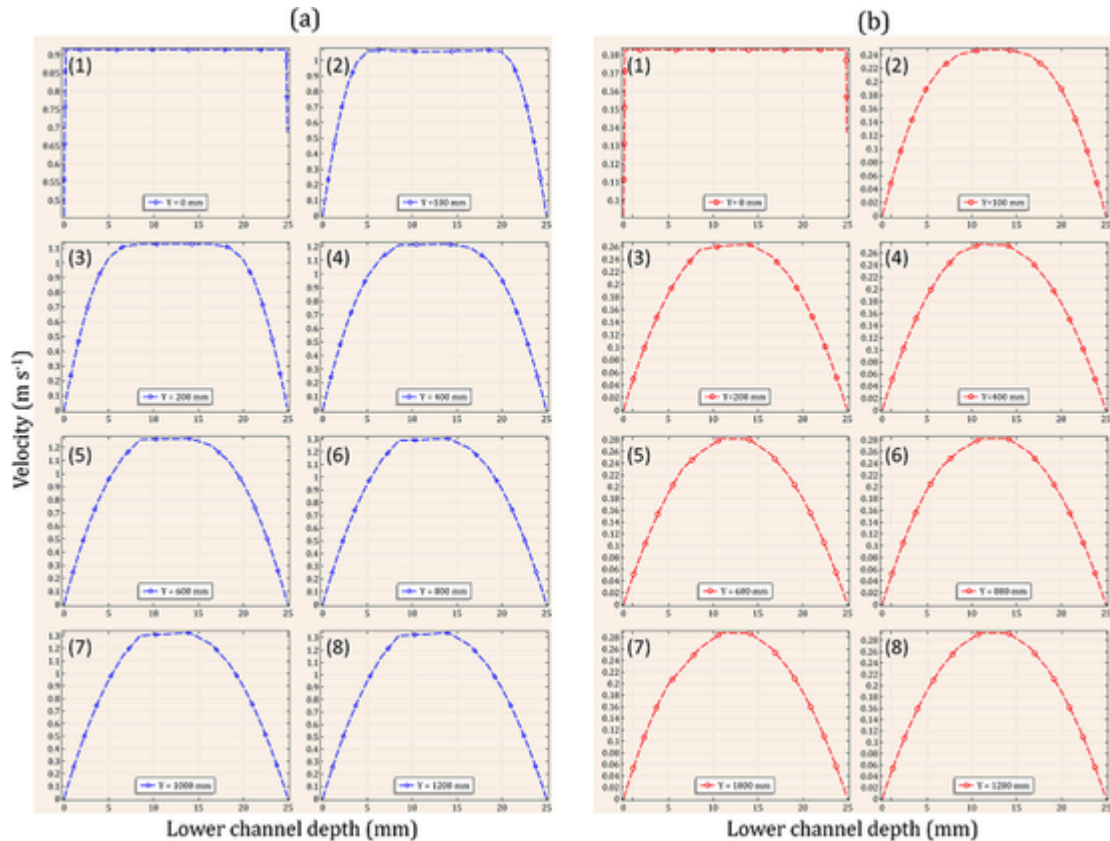
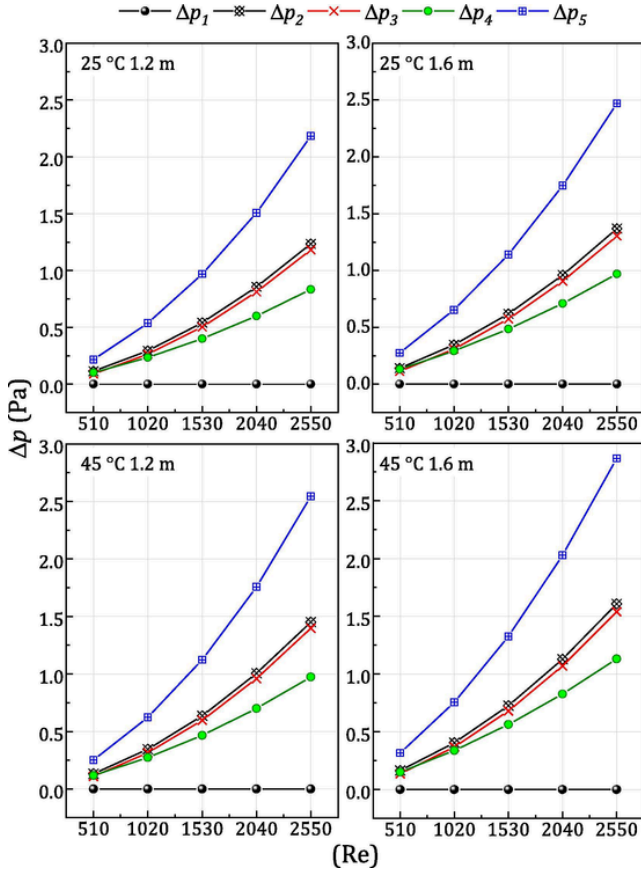


Fig. 4. Velocity profile for different locations along the lower air channel for flow Configuration 4 under laminar flow regime (a)  $Re = 510$ ,  $\bar{T} = 0.1829$  (m s<sup>-1</sup>),  $\dot{M} = 0.0041$  (kg s<sup>-1</sup>),  $L_{ent} = 0.549$  (b)  $Re = 2550$ ,  $\bar{T} = 0.9145$  (m s<sup>-1</sup>),  $\dot{M} = 0.0204$  (kg s<sup>-1</sup>),  $L_{ent} = 2.733$ .

**Table 3**

Design parameters for Configurations 2, 3, and 5. Configuration 4 parameters (mass flowrate, velocity and Re) are taken equal to half of those for Configurations 2, 3 and 5.

Design parameters for Configurations 2, 3 and 5									
$T_{amb}$	25 °C	45 °C	25 °C	45 °C	25 °C	45 °C	25 °C	45 °C	25 °C
$G$	1000 W m <sup>-2</sup>	1000 W m <sup>-2</sup>	1000 W m <sup>-2</sup>	1000 W m <sup>-2</sup>	1000 W m <sup>-2</sup>	1000 W m <sup>-2</sup>	1000 W m <sup>-2</sup>	1000 W m <sup>-2</sup>	1000 W m <sup>-2</sup>
$\delta_{D1}$	0.025 m	0.025 m	0.025 m	0.025 m	0.025 m	0.025 m	0.025 m	0.025 m	0.025 m
$\delta_{D2}$	0.025 m	0.025 m	0.025 m	0.025 m	0.025 m	0.025 m	0.025 m	0.025 m	0.025 m
$D_h$	0.0485 m	0.0485 m	0.0485 m	0.0485 m	0.0485 m	0.0485 m	0.0485 m	0.0485 m	0.0485 m
$L$	1.2 m	1.2 m	1.6 m	1.6 m	1.6 m	1.6 m	1.6 m	1.6 m	1.6 m
Re	$\bar{V}$	$\dot{M}_f$	$\bar{V}$	$\dot{M}_f$	$\bar{V}$	$\dot{M}_f$	$\bar{V}$	$\dot{M}_f$	$\dot{M}_f$
510	0.1633	0.0039	0.1829	0.0041	0.1633	0.0039	0.1829	0.0041	0.0041
1020	0.3265	0.0077	0.3658	0.0081	0.3265	0.0077	0.3658	0.0081	0.0081
1530	0.4898	0.0116	0.5487	0.0122	0.4898	0.0116	0.5487	0.0122	0.0122
2040	0.6530	0.0155	0.7316	0.0163	0.6530	0.0155	0.7316	0.0163	0.0163
2550	0.8163	0.0193	0.9145	0.0204	0.8163	0.0193	0.9145	0.0204	0.0204



**Fig. 5.** Pressure drop across the five PV/T arrangements versus Re (510–2550) using different lengths: (Left) 1.2 m and (Right) 1.6 m and inlet air temperatures (25 °C and 45 °C).

### 5.1. Optimisation strategy

In this section, we consider the optimisation of PV/T air system, subject to the conflicting objectives of minimising the fan power ( $P_{fan}$ ) and maximising the electrical power ( $P_{PV}$ ), whilst maximising the electric efficiency ( $\eta_{PV}$ ) and the thermal efficiency ( $\eta_{th}$ ). Three design variables are used, namely: the collector ( $L$ ), the depths of the lower air flow channel ( $\delta_{D1}$ ) and the upper air flow channel ( $\delta_{D2}$ ) in the ranges of  $0.6 \text{ m} \leq L \leq 1.3 \text{ m}$ ,  $0.004 \text{ m} \leq \delta_{D1} \leq 0.010 \text{ m}$  and  $0.004 \text{ m} \leq \delta_{D2} \leq 0.0015 \text{ m}$  (e.g. Table 1) with a constant Reynolds number of  $Re = 2550$ .

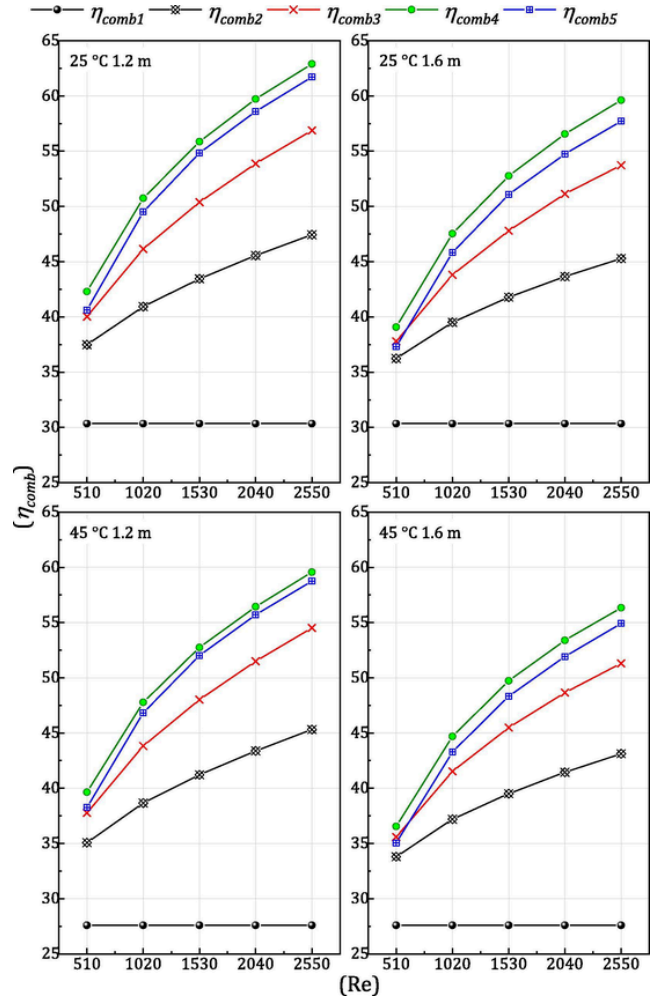


**Fig. 6.** Combined efficiencies versus Re (510–2550) for the five PV/T systems using different lengths (1.2 m and 1.6 m) and inlet air temperatures (25 °C and 45 °C).

The goal is to generate a Pareto front of non-dominated solutions, from which an appropriate compromise design can be reached. The Pareto front is obtained by building accurate metamodels of both  $P_{fan}$  and  $P_{PV}$  in one hand, and  $\eta_{PV}$  and  $\eta_{th}$  on the other hand, as a function of the three design variables. The metamodels are constructed using values of the  $P_{fan}$ ,  $P_{PV}$ ,  $\eta_{PV}$  and  $\eta_{th}$  from numerical simulations carried out at fifty Design of Experiments (DOE) points. These points are obtained using Optimal Latin Hypercubes (OLH), by means of a permutation genetic algorithm using the Audze-Eglais potential energy criterion to ensure an efficient distribution of DOE points. The points are laid out as uniformly as possible using criteria of minimising potential energy of repulsive forces which are inverse square functions of the separation of DOE points [71]:

$$\min E^{AE} = \min \sum_{i=1}^N \sum_{j=i+1}^N \frac{1}{L_{ij}^2}, \quad (17)$$

where  $L_{ij}$  is the Euclidian distance between points  $i$  and  $j$  ( $i \neq j$ ) and,  $N = 50$  is the number of DOE points. Fig. 7 (a), (b) and (c) reveal the uniform distribution of the DOE points within the design space as a combination of the design variables  $\delta_{D1}$ ,  $\delta_{D2}$  and  $L$ . Data summarising the fifty CFD simulations are available in Appendix C.

A Radial Basis Function (RBF) method is proven to be an effective design tool for a range of engineering applications, such as thermal air flow and wall-bounded flow systems [72–74]. RBF is used to build the

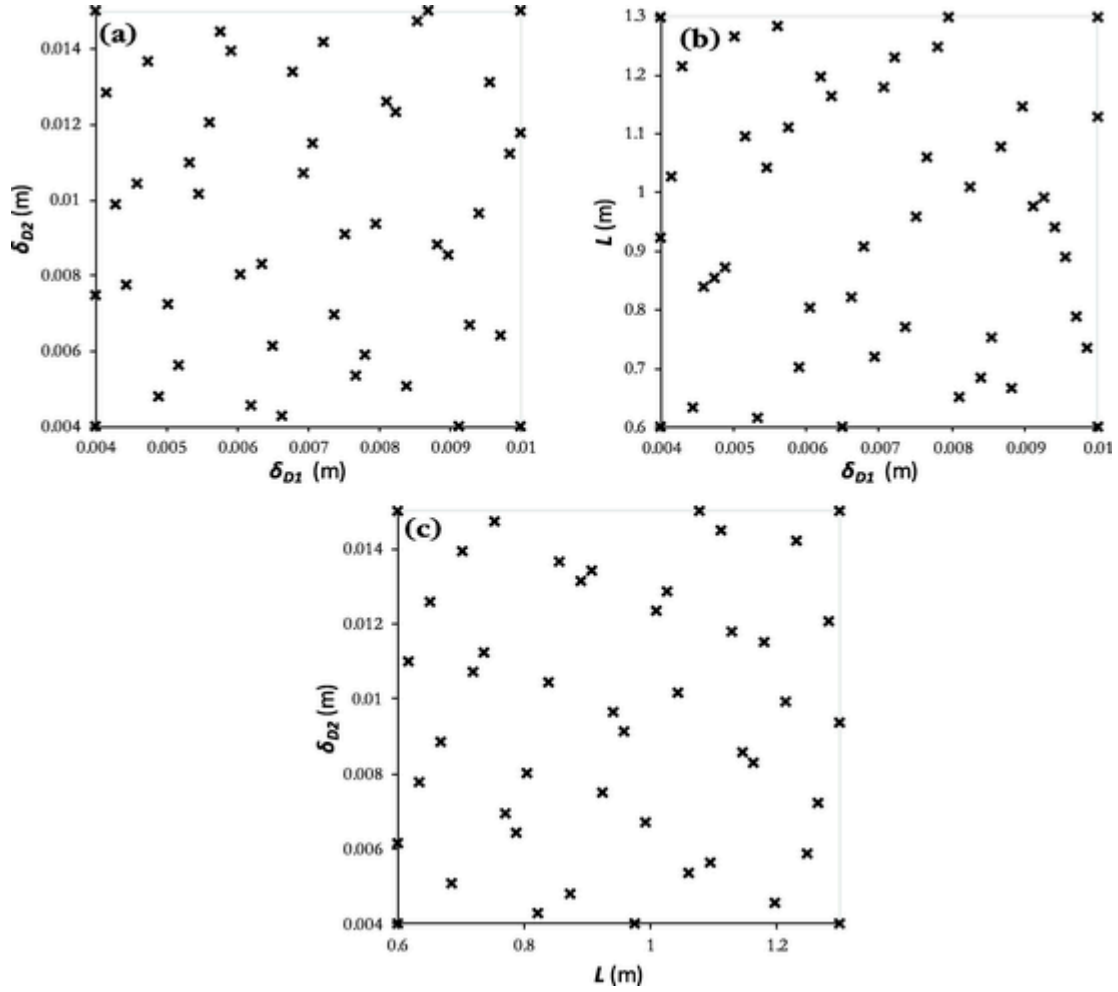


**Fig. 7.** Illustration of the DOE points: (a) Lower depth of flow ( $\delta_{D1}$ ) versus upper depth of flow  $\delta_{D2}$ , (b) Lower depth of flow ( $\delta_{D1}$ ) versus length of collector ( $L$ ), (c) Length of collector ( $L$ ) versus upper depth of flow ( $\delta_{D2}$ ).

metamodels for  $P_{fan}$  and  $P_{PV}$ , and  $\eta_{PV}$  and  $\eta_{th}$  throughout the design space where a cubic radial power function is used to determine the weighting ( $wg$ ) of points in the regression analysis at each point [75, 76]:

$$wg_i = r_i^3. \quad (18)$$

The parameter  $r_i$  is the normalised distance between the surrogate model prediction location from the  $i^{th}$  sampling point. The Pareto front is calculated using a multi-objective genetic algorithm (MOGA) approach based on [73,77,78]. Points on the Pareto front are non-dominated in the sense that it is not possible to decrease any of the objective functions (i.e.  $P_{fan}$  or  $P_{PV}$  and  $\eta_{PV}$  or  $\eta_{th}$ ) without increasing the other objective function. Hence, this provides designers the opportunity to select the most convenient compromise point among the optimum designs. In the next section, results of the optimisation analysis are discussed.

## 5.2. Optimisation analysis

As in previous studies (e.g. [13,79]), we first seek to maximise both the electric and the thermal efficiencies. This will then be followed by reformulating the optimisation problem to minimise the fan power consumption and maximise electrical power. The studies are also performed to investigate the significance of the temperature operating conditions, low temperature (25 °C) and high temperature (45 °C, see Tables C3 and C4). These two temperatures are found to be an appropriate

representation for low and high temperatures in the geographical regions under investigations. Illustrative examples of functions  $\eta_{PV}$  and  $\eta_{th}$  in terms of  $\delta_{D1}$ ,  $\delta_{D2}$  and  $L$  are presented in Figs. 8 and 9 respectively (e.g. See also Figs. C1 and C2, Appendix C).

Pareto front curve in Fig. 10 represents the results in terms of thermal and electrical efficiencies at 25 °C. The data reveal that any de-

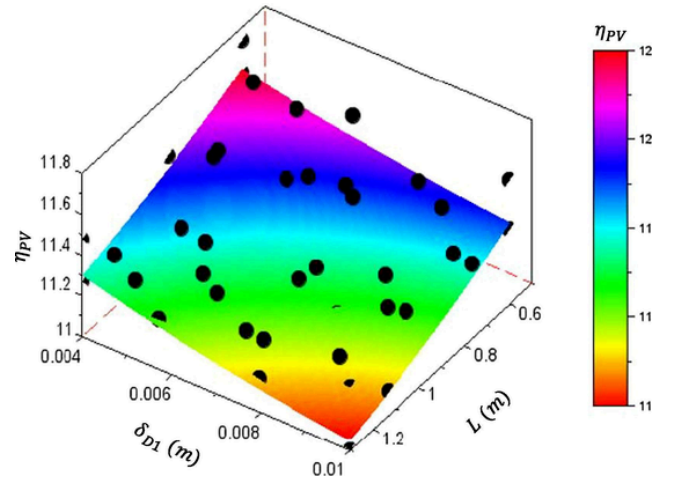


**Fig. 8.** Response surface function  $\eta_{PV}$  from the surrogate model at 25 °C together with the DOE points.



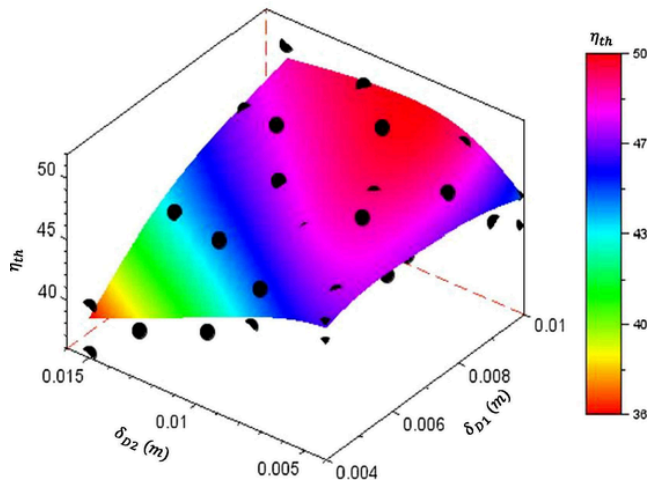


Fig. 9. Response surface function  $\eta_{th}$  from the surrogate model at 25 °C together with the DOE points.

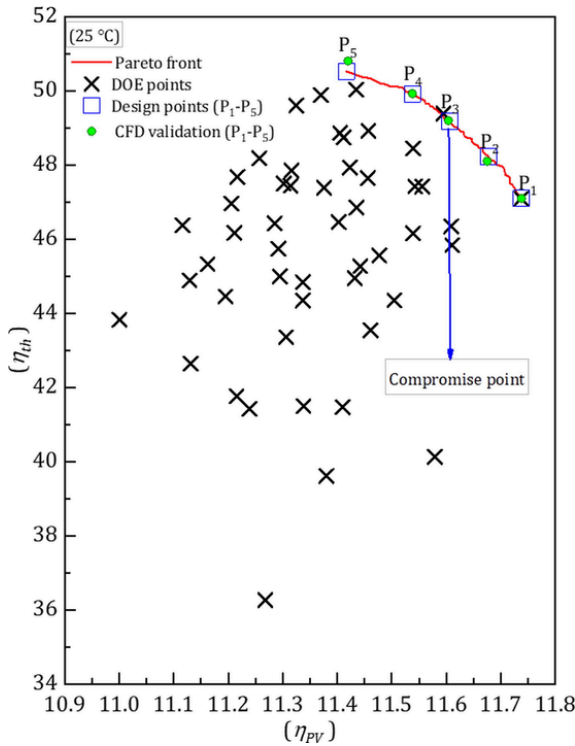


Fig. 10. Pareto front emphasising the compromise that can be struck in maximising both  $\eta_{th}$  and  $\eta_{PV}$  together with five representative design points (i.e. P1-P5) used for the PV/T performance analysis illustrated in Table 4 at 25 °C.

Table 4

PV/T design performance of Configuration 4 at five operating condition points located on the Pareto together with CFD validation, as plotted in Fig. 10 when operating at 25 °C. Relative error =  $|\eta_{metamodels} - \eta_{CFD}| \times 100 / \eta_{metamodels}$ .

Design points for Pareto front				Metamodels		CFD validation		Relative error	
Point	L (m)	$\delta_{D1}$ (m)	$\delta_{D2}$ (m)	$\eta_{th}$	$\eta_{PV}$	$\eta_{th}$	$\eta_{PV}$	$\eta_{th}$ (%)	$\eta_{PV}$ (%)
P <sub>1</sub>	0.6000	0.0100	0.0110	50.5326	11.4169	50.8080	11.4200	0.5450	0.0272
P <sub>2</sub>	0.6089	0.0076	0.0071	49.9194	11.5383	49.9310	11.5380	0.0232	0.0026
P <sub>3</sub>	0.6080	0.0064	0.0057	49.1889	11.6064	49.2010	11.6040	0.0246	0.0207
P <sub>4</sub>	0.6074	0.0053	0.0044	48.2299	11.6777	48.1070	11.6750	0.2548	0.0231
P <sub>5</sub>	0.6000	0.0040	0.0040	47.0980	11.7380	47.0970	11.7380	0.0022	0.0000

crease of  $\eta_{PV}$  or  $\eta_{th}$  is followed by an increase of the other objective function. Table 4 lists five sample points on the Pareto front (P<sub>1</sub>-P<sub>5</sub>) and a comparison between the calculated values of  $\eta_{PV}$  and  $\eta_{th}$  from the metamodels at these points and from the full CFD numerical simulations. A very good agreement between the metamodel and full numerical predictions occurs in all cases, demonstrating the accuracy of the metamodeling approach implemented. This is confirmed by a maximum relative error obtained for  $\eta_{PV}$  and  $\eta_{th}$  are 0.5420% and 0.0272%, respectively.

Table 4 also contains the compromise that must be struck between high  $\eta_{PV}$  and high  $\eta_{th}$ . For example, point P<sub>3</sub> is a good compromise with a thermal and electrical efficiency of 49.2 and 11.6 respectively with corresponding  $L=0.6080$  m,  $\delta_{D1}=0.0064$  m and  $\delta_{D2}=0.0057$  m.

In Fig. 10, the Pareto front emphasising the compromise that can be struck in maximising both  $\eta_{th}$  and  $\eta_{PV}$  together with five representative design points (P<sub>1</sub>-P<sub>5</sub>) used for the PV/T performance analysis illustrated in Table 4 at 25 °C. At 45 °C, the findings (see Appendix C, Fig. C3 and Table C3) are similar to the low temperature scenario. Results between the metamodels and full CFD calculations agree well. Point P<sub>3</sub> in Table C3, which corresponds to a thermal efficiency of 49.0 and an electrical efficiency of 10.6, and is found to be good design (i.e.  $L=0.6131$  m,  $\delta_{D1}=0.0065$  m and  $\delta_{D2}=0.0058$  m). The design optimisation is undertaken in terms of flow and electrical powers, with aim to simultaneously minimise  $P_{fan}$  and maximise  $P_{PV}$ . The resulting Pareto for the 25 °C temperature condition is presented in Table 5 and illustrated in Fig. 11.

Fig. 11 and Table 5 show a sample of five points on the Pareto front (P<sub>1</sub>-P<sub>5</sub>) at 25 °C. A comparison between the values of  $P_{PV}$  and  $P_{fan}$  is determined from the metamodels at these points and the full CFD numerical simulations. There is a good agreement between the metamodel and full numerical predictions for all cases, demonstrating the accuracy of the metamodeling approach implemented. This has been justified by the maximum relative errors obtained for  $P_{PV}$  and  $P_{fan}$  of 8.7514% and 0.2871%, respectively.

Table 5 also reveals that point P<sub>3</sub> to be a good compromise design. Lastly, a significant result can be drawn from the Pareto curve which is the impact of the fan power  $P_{fan}$  on the power generation  $P_{PV}$ . An increase of fan power  $P_{fan}$  just after the compromised point P<sub>3</sub> causes the PV/T power generation to be negligible as  $P_{PV}$  tends to plateau. Similar findings are obtained for 45 °C (e.g. See Fig. C4 and Table C4, Appendix C).

From Table 5, there is a clear trend of a slight increase in electrical power generation compared to huge increase in fan power consumption after P<sub>3</sub>. It should be mentioned that the main variables affecting the electrical power generation are the collector dimensions (length, depth of flows).

## 6. Conclusion

A computational fluid dynamics multi-objective optimisation framework analysis is made to evaluate photovoltaic/thermal air systems. Three main objectives are conducted to obtain the optimal design: A) selection of design parameters; and B) performing preliminary

**Table 5**

PV/T design performance of Configuration 4 at five operating condition points located on the Pareto together with CFD validation, as shown in Fig. 11 when operating at 25 °C. Relative error =  $|P_{\text{metamodels}} - P_{\text{CFD}}| \times 100 / P_{\text{metamodels}}$

Design points for Pareto front				Metamodels		CFD validation		Relative Error	
Point	L (m)	$\delta_{D1}$ (m)	$\delta_{D2}$ (m)	$P_{\text{fan}}$ (W)	$P_{PV}$ (W)	$P_{\text{fan}}$ (W)	$P_{PV}$ (W)	$P_{\text{fan}}$ (%)	$P_{PV}$ (%)
P <sub>1</sub>	0.6000	0.0100	0.0150	0.9904	40.7680	0.9566	40.7480	3.4128	0.0491
P <sub>2</sub>	0.9756	0.0100	0.0150	1.1578	64.9089	1.1697	64.8840	1.0278	0.0384
P <sub>3</sub>	1.3000	0.0100	0.0149	1.4056	85.4630	1.3588	85.4010	3.3295	0.0725
P <sub>4</sub>	1.2987	0.0059	0.0046	12.6832	88.3088	11.6000	88.1170	8.5404	0.2172
P <sub>5</sub>	1.3000	0.0040	0.0040	22.9220	89.1630	20.9160	88.9070	8.7514	0.2871

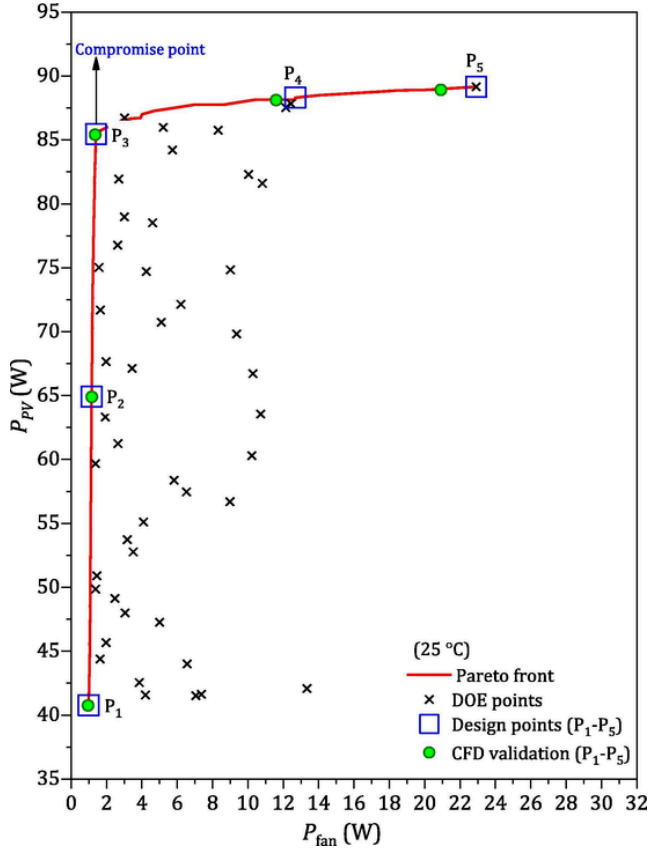


**Fig. 11.** Pareto front showing the compromise that can be achieved in minimising  $P_{\text{fan}}$  and maximising  $P_{PV}$  together with five representative design points (e.g. P<sub>1</sub>-P<sub>5</sub>) used for the PV/T performance analysis illustrated in when Table 5 operating at 25 °C.

parametric studies of five common configurations (1: a standard photovoltaic system without active cooling, 2: single pass duct, 3: a single pass duct (glazed), 4: 2 co-current pass ducts and 5: a double-pass single duct). Configuration 4 has the relatively best thermal performance: total efficiency and lowest fan power consumption (lowest pressure drop). Therefore, this configuration is identified as the best conventional photovoltaic and thermal collection to test for any further design improvements in the optimisation investigation.

In the optimisation of Configuration 4, the following five main steps are considered: 1) formulation of the objective functions to maximise both electric and thermal efficiencies; 2) parameterised objective functions in terms of three variables, the length of collector and the depths of the lower and upper air flow channels; 3) design of experiments using optimal Latin hypercube method as inputs for the computational fluid dynamic simulations; 4) generating the metamodels from design of experiment points (step 3); and 5) using a genetic algorithm method to obtain Pareto front curves. In step 5, four Pareto front curves are presented for the design optimisations, two curves for the analysis of the thermal and electric efficiencies at 25 °C and 45 °C and two curves for analysis of the fan and electrical power at 25 °C and 45 °C. The thermal and electric efficiencies are improved from 44.5% to 50.1% and from 10.0% to 10.5%, respectively.

#### Declaration of Competing Interest

The authors declare that they have no known competing financial interests or personal relationships that could have appeared to influence the work reported in this paper.

#### Appendix A. Air properties

The set of empirical Correlations (A1) – (A7) used to estimate the air properties, which are functions of bulk fluid temperature and proportionally non-linear [38,80]. These correlations are applicable in the temperature range –73 °C to 127 °C.

$$\mu = -8.39e^{-7} + 8.36e^{-8}T_f - 7.695e^{-11}T_f^2 + 4.65e^{-14}T_f^3 - 1.07e^{-17}T_f^4, \quad (\text{A1})$$

$$\rho = 3.9147 - 0.01608T_f + (2.9013e^{-5}T_f^2) - (1.9407e^{-5}T_f^3), \quad (\text{A2})$$

$$v = \mu / \rho, \quad (\text{A3})$$

$$k = -0.0023 + 1.155e^{-4}T_f - 7.91e^{-8}T_f^2 + 4.118e^{-11}T_f^3 - 7.44e^{-15}T_f^4, \quad (\text{A4})$$

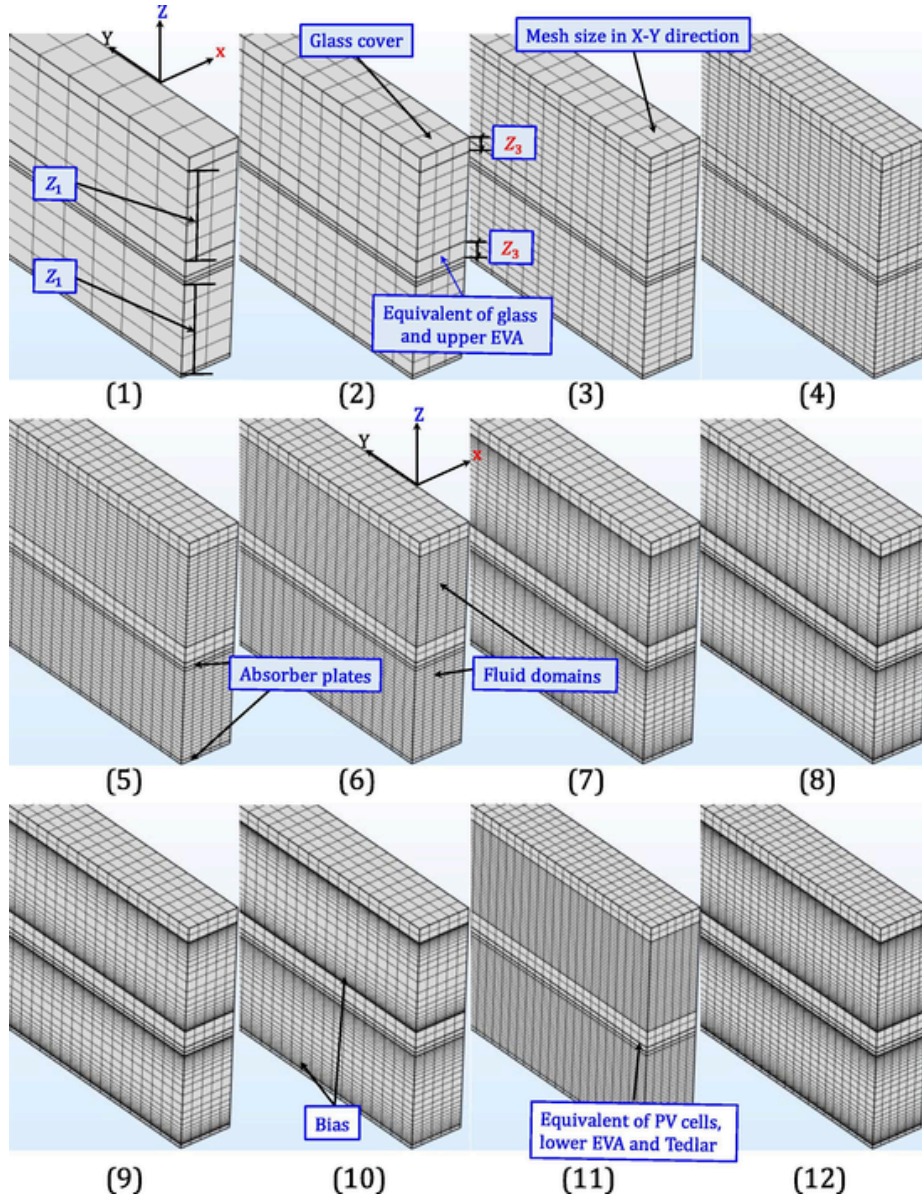


Fig. B1. Grid independence test for Configuration 4 using hexahedral mesh element type.

$$c_p = 1047.7 - 0.373T_f + 9.46e^{-4}T_f^2 - 6.03e^{-7}T_f^3 + 1.29e^{-10}T_f^4, \quad (A5)$$

$$\alpha = k/\rho C_p, \quad (A6)$$

$$\text{Pr} = \nu/\alpha. \quad (A7)$$

## Appendix B. Grid independence check

See Fig. B1 and Table B1.

## Appendix C. Optimisation strategy

In Tables C1 and C2,  $L$  is the length of the channel/collector,  $\delta_{D1}$  and  $\delta_{D2}$  are the lower and upper depth of flows (m) and,  $\bar{V}_L$  and  $\bar{V}_U$  are the lower and upper mean inlet velocities ( $\text{m s}^{-1}$ ) respectively (see Figs. C1–C4 and Table C3 and C4)

**Table B1**

Mesh independent test analysis for two conditions ( $Re = 510$ ,  $\bar{\nu} = 0.1829$  (m s<sup>-1</sup>),  $\dot{M}_f = 0.0041$  (kg s<sup>-1</sup>)) and ( $Re = 2550$ ,  $\bar{\nu} = 0.9145$  (m s<sup>-1</sup>),  $\dot{M}_f = 0.0204$  (kg s<sup>-1</sup>)).

Trial No	NOE	RAM	t	DOF	MEQ	$T_{mpv}$	$\eta_{th}$	$\Delta p_f$	$T_{fo}$
Re = 510, $\bar{\nu} = 0.1829$ (m s <sup>-1</sup> ), $\dot{M}_f = 0.0041$ (kg s <sup>-1</sup> )									
1	3360	1.81	41	22,713	1	86.48	24.08	0.207	73.85
2	9804	3.30	277	60,204	1	86.31	23.54	0.207	73.28
3	19,401	5.45	265	115,584	1	86.11	23.08	0.207	72.74
4	64,935	21.56	1759	358,716	1	86.02	22.90	0.211	72.52
5	78,225	23.67	1706	438,876	1	86.00	22.91	0.213	72.53
6	94,905	24.30	1792	539,076	1	85.97	22.84	0.214	72.45
7	94,905	24.48	1752	539,076	1	85.88	22.70	0.220	72.28
8	94,905	25.97	1787	539,076	1	85.86	22.67	0.222	72.25
9	94,905	26.81	1755	539,076	1	85.84	22.66	0.223	72.23
10	94,905	27.03	1759	539,076	1	85.82	22.65	0.224	72.22
11	169,242	60.80	6397	942,326	1	85.95	22.80	0.216	72.40
12	169,242	64.61	8866	942,326	1	85.85	22.66	0.222	72.23
Re = 2550, $\bar{\nu} = 0.9145$ (m s <sup>-1</sup> ), $\dot{M}_f = 0.0204$ (kg s <sup>-1</sup> )									
1	3360	1.85	44	22,713	1	75.90	46.36	1.408	56.20
2	9804	3.4	295	60,204	1	75.96	45.35	1.403	55.96
3	19,401	5.59	264	115,584	1	75.97	44.37	1.429	55.72
3a	44,823	8.09	352	285,824	1	75.74	43.11	1.56	55.42
3ab	44,823	8.84	346	285,824	1	75.83	43.43	1.50	55.50
3abc	51,513	9.49	382	330,624	1	75.81	43.36	1.51	55.48
3abcd	51,513	9.49	385	330,624	1	75.75	43.10	1.57	55.42
4	64,935	20.97	1586	358,716	1	75.90	43.87	1.46	55.60
5	78,225	22.23	1642	438,876	1	75.87	43.65	1.48	55.55
6	94,905	25.98	1827	539,076	1	75.84	43.52	1.49	55.51
7	94,905	27.18	1780	539,076	1	75.75	43.20	1.54	55.44
7a	111,555	27.21	2014	639,276	1	75.74	43.12	1.56	55.42
7ab	111,555	27.32	1969	639,276	1	75.83	43.43	1.50	55.50
7abc	128,205	28.87	2128	739,476	1	75.81	43.37	1.51	55.48
7abcd	128,205	27.97	2290	739,476	1	75.74	43.11	1.56	55.42
8	94,905	26.36	1757	539,076	1	75.73	43.15	1.55	55.43
9	94,905	23.85	1746	539,076	1	75.71	43.10	1.557	55.42
10	94,905	25.66	1807	539,076	1	75.69	43.07	1.563	55.41
11	169,242	61.51	7368	942,326	1	75.83	43.44	1.504	55.50
12	169,242	63.74	8378	942,326	1	75.73	43.12	1.558	55.42



**Table C1**

Fifty DOE points and their CFD results for four objective functions of Configuration 4 for low temperature weather (25 °C).

$L$ (m)	$\delta_{D1}$ (m)	$\delta_{D2}$ (m)	$\bar{V}_L$ (m s <sup>-1</sup> )	$\bar{V}_U$ (m s <sup>-1</sup> )	$\dot{M}_f$ (kg s <sup>-1</sup> )	$\eta_{th}$	$\eta_{PV}$	$P_{fan}$ (W)	$P_{PV}$ (W)
0.6	0.004	0.004	4.97	4.97	0.0377	47.10	11.74	13.34	42.09
0.6	0.01	0.004	2.00	4.97	0.0378	45.84	11.61	7.37	41.63
0.6	0.004	0.015	4.97	1.34	0.0380	40.12	11.58	7.05	41.52
0.6	0.01	0.015	2.00	1.34	0.0381	49.89	11.37	0.99	40.77
1.3	0.004	0.004	4.97	4.97	0.0377	45.56	11.48	22.92	89.16
1.3	0.01	0.004	2.00	4.97	0.0378	43.36	11.31	12.44	87.84
1.3	0.004	0.015	4.97	1.34	0.0380	36.26	11.27	12.14	87.54
1.3	0.01	0.015	2.00	1.34	0.0381	43.83	11.00	1.40	85.45
0.92439	0.004	0.00749	4.97	2.67	0.0378	44.35	11.51	10.72	63.55
1.0268	0.00415	0.01285	4.79	1.57	0.0379	39.61	11.38	9.36	69.83
1.2146	0.00429	0.0099	4.64	2.02	0.0378	41.50	11.34	10.04	82.30
0.63415	0.00444	0.00776	4.48	2.58	0.0378	46.34	11.61	6.56	44.00
0.83902	0.00459	0.01044	4.34	1.92	0.0379	43.54	11.46	6.52	57.47
0.8561	0.00473	0.01366	4.21	1.47	0.0379	41.47	11.41	5.82	58.37
0.87317	0.00488	0.0048	4.08	4.15	0.0377	47.42	11.56	10.22	60.30
1.2659	0.00502	0.00722	3.97	2.77	0.0378	44.84	11.34	8.32	85.76
1.0951	0.00517	0.00561	3.85	3.55	0.0378	46.86	11.44	9.01	74.83
0.61707	0.00532	0.01098	3.74	1.83	0.0379	46.17	11.54	3.85	42.55
1.0439	0.00546	0.01017	3.65	1.97	0.0379	44.35	11.34	5.10	70.73
1.2829	0.00561	0.01205	3.55	1.67	0.0379	41.77	11.22	5.21	85.98
1.1122	0.00576	0.01446	3.46	1.39	0.0380	41.42	11.24	4.25	74.70
0.70244	0.0059	0.01393	3.38	1.45	0.0380	44.95	11.43	3.05	47.99
0.80488	0.00605	0.00802	3.30	2.49	0.0378	47.66	11.46	4.09	55.10
1.1976	0.0062	0.00454	3.22	4.38	0.0378	46.47	11.40	10.81	81.61
1.1634	0.00634	0.00829	3.15	2.41	0.0378	45.75	11.29	4.60	78.51
0.6	0.00649	0.00615	3.07	3.24	0.0378	49.39	11.60	4.20	41.58
0.82195	0.00663	0.00427	3.01	4.66	0.0378	47.43	11.54	8.98	56.70
0.90732	0.00678	0.01339	2.94	1.50	0.0380	45.00	11.30	2.64	61.24
0.71951	0.00693	0.01071	2.88	1.87	0.0379	47.93	11.42	2.48	49.12
1.1805	0.00707	0.01151	2.82	1.74	0.0379	44.45	11.20	3.01	78.98
1.2317	0.00722	0.0142	2.77	1.42	0.0380	42.64	11.13	2.69	81.93
0.77073	0.00737	0.00695	2.71	2.87	0.0378	48.93	11.46	3.51	52.77
0.95854	0.00751	0.0091	2.66	2.20	0.0379	47.45	11.31	2.84	64.81
1.061	0.00766	0.00534	2.61	3.73	0.0378	47.39	11.38	6.21	72.13
1.2488	0.0078	0.00588	2.56	3.39	0.0378	46.43	11.29	5.73	84.21
1.3	0.00795	0.00937	2.51	2.14	0.0379	45.33	11.16	3.02	86.72
0.65122	0.0081	0.01259	2.47	1.60	0.0380	48.87	11.41	1.63	44.39
1.0098	0.00824	0.01232	2.43	1.63	0.0380	46.17	11.21	1.97	67.65
0.68537	0.00839	0.00507	2.38	3.93	0.0378	48.46	11.54	5.00	47.26
0.75366	0.00854	0.01473	2.34	1.37	0.0381	47.51	11.30	1.45	50.90
1.0781	0.00868	0.015	2.31	1.34	0.0381	44.89	11.13	1.65	71.70
0.66829	0.00883	0.00883	2.27	2.27	0.0379	50.04	11.44	1.97	45.67
1.1463	0.00898	0.00856	2.23	2.34	0.0379	46.97	11.21	2.63	76.77
0.97561	0.00912	0.004	2.20	4.97	0.0378	45.27	11.44	10.28	66.71
0.99268	0.00927	0.00668	2.16	2.99	0.0379	47.85	11.32	3.45	67.13
0.94146	0.00941	0.00963	2.13	2.08	0.0380	48.19	11.26	1.93	63.33
0.89024	0.00956	0.01312	2.10	1.53	0.0380	47.68	11.22	1.37	59.67
0.7878	0.00971	0.00641	2.06	3.11	0.0379	48.75	11.41	3.17	53.72
0.73659	0.00985	0.01124	2.03	1.79	0.0380	49.61	11.33	1.38	49.85
1.1293	0.01	0.01178	2.00	1.71	0.0380	46.38	11.12	1.57	75.02

**Table C2**

Fifty DOE points and their CFD results for four objective functions of Configuration 4 for high temperature weather (45 °C).

$L$ (m)	$\delta_{D1}$ (m)	$\delta_{D2}$ (m)	$\bar{V}_L$ (m s <sup>-1</sup> )	$\bar{V}_U$ (m s <sup>-1</sup> )	$\dot{M}_f$ (kg s <sup>-1</sup> )	$\eta_{th}$	$\eta_{PV}$	$P_{fan}$ (W)	$P_{PV}$ (W)
0.6	0.004	0.004	5.57	5.57	0.0397	46.45	10.76	17.55	38.57
0.6	0.01	0.004	2.24	5.57	0.0398	45.59	10.64	9.69	38.14
0.6	0.004	0.015	5.57	1.51	0.0399	39.49	10.61	9.26	38.04
0.6	0.01	0.015	2.24	1.51	0.0401	49.44	10.42	1.30	37.35
1.3	0.004	0.004	5.57	5.57	0.0397	45.10	10.51	30.05	81.67
1.3	0.01	0.004	2.24	5.57	0.0398	43.27	10.36	16.32	80.45
1.3	0.004	0.015	5.57	1.51	0.0399	35.50	10.32	15.86	80.20
1.3	0.01	0.015	2.24	1.51	0.0401	43.12	10.08	1.83	78.33
0.92439	0.004	0.00749	5.57	2.99	0.0398	43.73	10.54	14.06	58.23
1.0268	0.00415	0.01285	5.37	1.75	0.0399	38.90	10.43	12.26	63.98
1.2146	0.00429	0.0099	5.20	2.27	0.0398	40.90	10.39	13.35	75.41
0.63415	0.00444	0.00776	5.02	2.88	0.0398	45.77	10.64	8.65	40.33
0.83902	0.00459	0.01044	4.86	2.15	0.0398	42.95	10.51	8.61	52.68
0.8561	0.00473	0.01366	4.71	1.65	0.0399	40.82	10.46	7.70	53.51
0.87317	0.00488	0.0048	4.57	4.65	0.0397	47.11	10.59	13.44	55.28
1.2659	0.00502	0.00722	4.44	3.10	0.0398	44.37	10.39	10.97	78.57
1.0951	0.00517	0.00561	4.32	3.98	0.0397	46.40	10.48	11.85	68.56
0.61707	0.00532	0.01098	4.19	2.05	0.0399	45.79	10.57	5.08	38.99
1.0439	0.00546	0.01017	4.09	2.21	0.0399	43.77	10.39	6.70	64.81
1.2829	0.00561	0.01205	3.98	1.87	0.0399	41.19	10.28	6.83	78.78
1.1122	0.00576	0.01446	3.88	1.56	0.0400	40.89	10.30	5.58	68.46
0.70244	0.0059	0.01393	3.79	1.62	0.0400	44.36	10.48	4.03	43.98
0.80488	0.00605	0.00802	3.69	2.79	0.0398	47.28	10.50	5.37	50.49
1.1976	0.0062	0.00454	3.60	4.91	0.0397	46.32	10.45	14.15	74.77
1.1634	0.00634	0.00829	3.52	2.70	0.0398	45.40	10.35	6.02	71.93
0.6	0.00649	0.00615	3.44	3.63	0.0398	49.15	10.63	5.54	38.10
0.82195	0.00663	0.00427	3.37	5.22	0.0397	47.10	10.58	11.90	51.96
0.90732	0.00678	0.01339	3.30	1.68	0.0400	44.39	10.35	3.46	56.12
0.71951	0.00693	0.01071	3.23	2.10	0.0399	47.47	10.47	3.26	45.01
1.1805	0.00707	0.01151	3.16	1.95	0.0399	43.97	10.26	3.96	72.37
1.2317	0.00722	0.0142	3.10	1.59	0.0400	42.03	10.20	3.54	75.09
0.77073	0.00737	0.00695	3.04	3.22	0.0398	48.63	10.50	4.61	48.35
0.95854	0.00751	0.0091	2.98	2.46	0.0399	46.91	10.37	3.72	59.39
1.061	0.00766	0.00534	2.92	4.18	0.0398	46.98	10.42	8.20	66.09
1.2488	0.0078	0.00588	2.87	3.80	0.0398	46.29	10.34	7.51	77.16
1.3	0.00795	0.00937	2.82	2.39	0.0399	44.88	10.23	3.96	79.46
0.65122	0.0081	0.01259	2.76	1.79	0.0400	48.41	10.45	2.14	40.67
1.0098	0.00824	0.01232	2.72	1.83	0.0400	45.56	10.27	2.59	61.99
0.68537	0.00839	0.00507	2.67	4.40	0.0398	48.18	10.57	6.61	43.30
0.75366	0.00854	0.01473	2.62	1.53	0.0400	46.96	10.36	1.90	46.64
1.0781	0.00868	0.015	2.58	1.51	0.0401	44.12	10.20	2.17	65.71
0.66829	0.00883	0.00883	2.54	2.54	0.0399	49.70	10.48	2.59	41.84
1.1463	0.00898	0.00856	2.50	2.62	0.0399	46.48	10.27	3.46	70.35
0.97561	0.00912	0.004	2.46	5.57	0.0398	44.93	10.48	13.51	61.11
0.99268	0.00927	0.00668	2.42	3.35	0.0399	47.44	10.37	4.53	61.51
0.94146	0.00941	0.00963	2.38	2.33	0.0399	47.62	10.32	2.54	58.04
0.89024	0.00956	0.01312	2.35	1.72	0.0400	47.04	10.28	1.80	54.68
0.7878	0.00971	0.00641	2.31	3.49	0.0399	48.47	10.46	4.18	49.23
0.73659	0.00985	0.01124	2.28	2.00	0.0400	49.13	10.38	1.81	45.68
1.1293	0.01	0.01178	2.24	1.91	0.0400	45.83	10.19	2.07	68.75

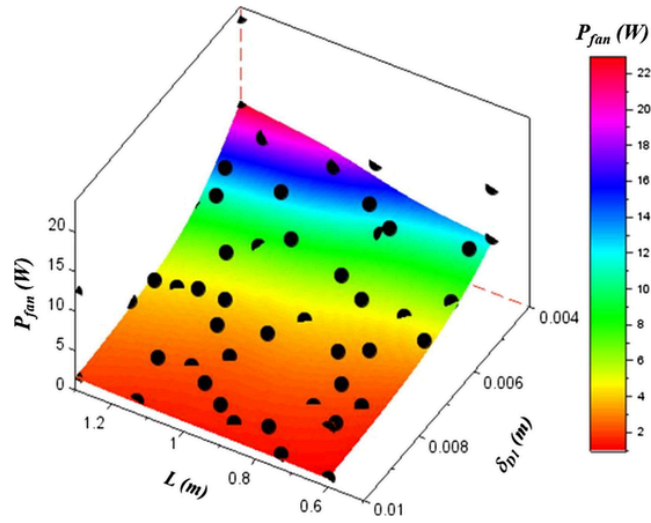


Fig. C1. Response surface function  $\eta_{th}$  from the surrogate model at 25 °C together with the DOE points.

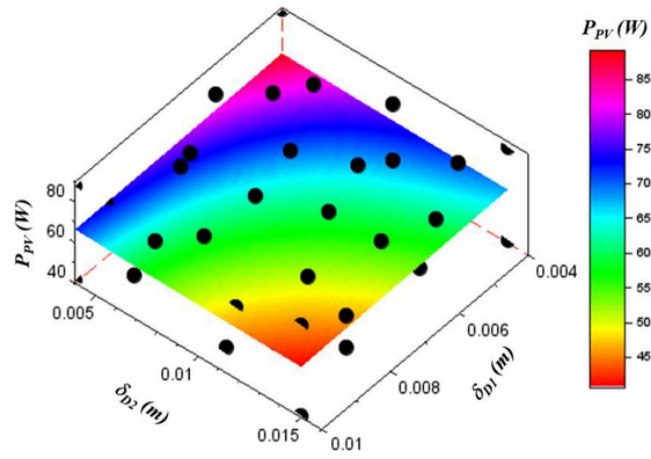
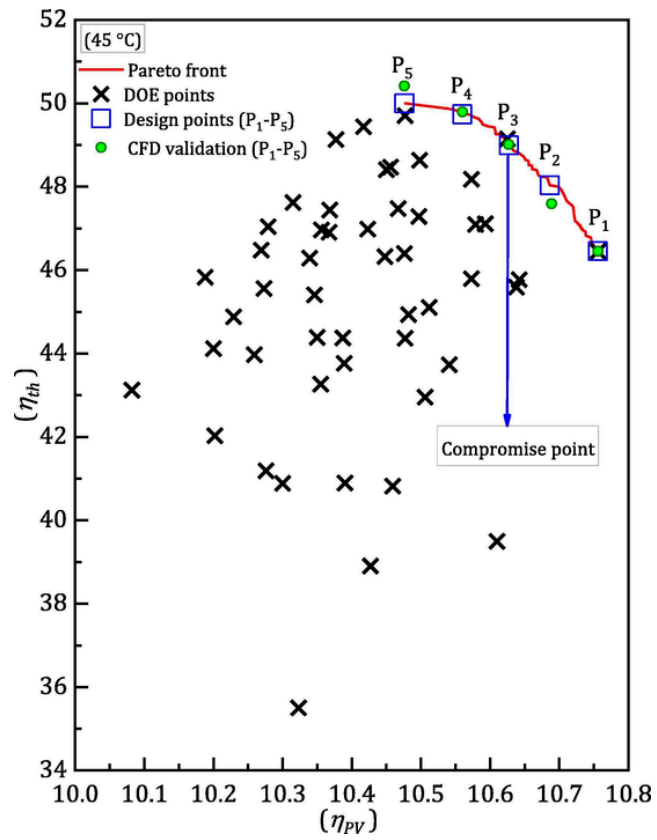


Fig. C2. Response surface function  $P_{PV}$  from the surrogate model at 25 °C together with the DOE points.



**Fig. C3.** Pareto front emphasising the compromise that can be struck in maximising both  $\eta_{th}$  and  $\eta_{PV}$  together with five representative design points (P1-P5) used for the PV/T performance analysis illustrated in Table C3 at 45 °C.



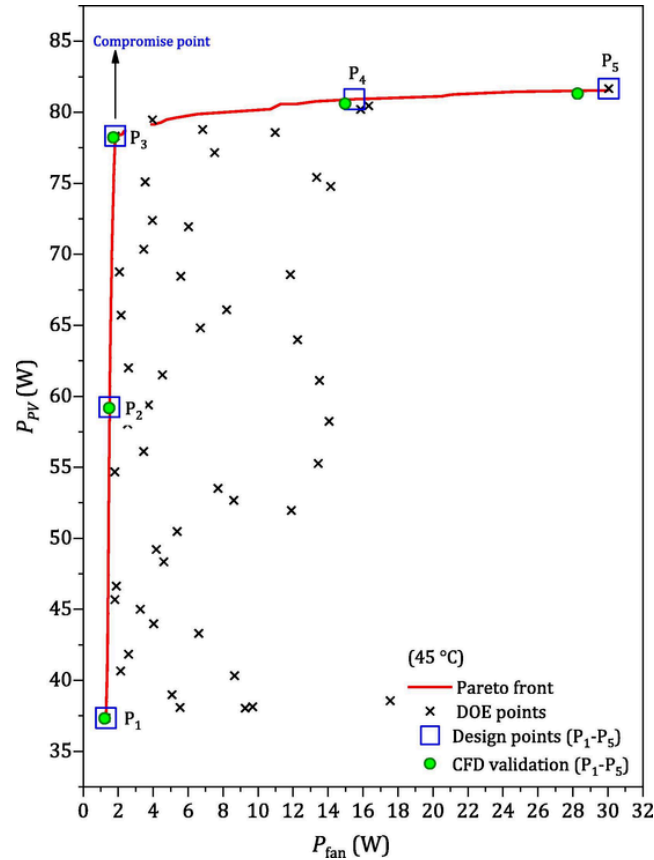


Fig. C4. Pareto front showing the compromises that can be struck in minimising  $P_{fan}$  and maximising  $P_{PV}$  together with five representative design points (e.g.  $P_1$ - $P_5$ ) used for the PV/T performance analysis illustrated in Table C4 when operating at 45 °C.

Table C3

PV/T efficiencies of Configuration 4 at five operating conditions points located on the Pareto front together with their CFD verification at 45 °C, as shown in Fig.

C3. Relative error =  $|\eta_{metamodels} - \eta_{CFD}| \times 100 / \eta_{metamodels}$ .

Design points for Pareto front				Metamodels		CFD		Relative Error	
Point	L (m)	$\delta_{D1}$ (m)	$\delta_{D2}$ (m)	$\eta_{th}$	$\eta_{PV}$	$\eta_{th}$	$\eta_{PV}$	$\eta_{th}$ (%)	$\eta_{PV}$ (%)
P <sub>1</sub>	0.6171	0.0100	0.0094	50.0005	10.4761	50.4130	10.4760	0.8250	0.0010
P <sub>2</sub>	0.6134	0.0081	0.0071	49.7368	10.5598	49.7930	10.5600	0.1130	0.0019
P <sub>3</sub>	0.6131	0.0065	0.0058	48.9896	10.6273	49.0110	10.6270	0.0437	0.0028
P <sub>4</sub>	0.6181	0.0059	0.0042	48.0327	10.6863	47.5910	10.6890	0.9196	0.0253
P <sub>5</sub>	0.6000	0.0040	0.0040	46.4510	10.7560	46.4510	10.7560	0.0000	0.0000

Table C4

PV/T design performance of Configuration 4 at five operating conditions points located on the Pareto front together with CFD verification at 45 °C. Relative error

=  $|P_{metamodels} - P_{CFD}| \times 100 / P_{metamodels}$ .

Design points for Pareto front				Metamodels		CFD		Relative Error	
Point	L (m)	$\delta_{D1}$ (m)	$\delta_{D2}$ (m)	$P_{fan}$ (W)	$P_{PV}$ (W)	$P_{fan}$ (W)	$P_{PV}$ (W)	$P_{fan}$ (%)	$P_{PV}$ (%)
P <sub>1</sub>	0.6000	0.0100	0.0150	1.3023	37.3500	1.2268	37.3160	5.7974	0.0910
P <sub>2</sub>	0.9712	0.0100	0.0150	1.5125	59.2303	1.4887	59.1710	1.5736	0.1001
P <sub>3</sub>	1.3000	0.0100	0.0150	1.8333	78.3270	1.7297	78.2150	5.6510	0.1430
P <sub>4</sub>	1.2996	0.0052	0.0055	15.5108	80.9034	14.9800	80.5970	3.4221	0.3787
P <sub>5</sub>	1.3000	0.0040	0.0040	30.0530	81.6650	28.2670	81.2990	5.9428	0.4482

## References

- [1] H.G. Teo, P.S. Lee, M.N.A. Hawlader, An active cooling system for photovoltaic modules, Appl. Energy 90 (2012) 309–315, <https://doi.org/10.1016/j.apenergy.2011.01.017>.
- [2] X. Zhang, X. Zhao, S. Smith, J. Xu, X. Yu, Review of R&D progress and practical application of the solar photovoltaic/thermal (PV/T) technologies, Renew. Sustain. Energy Rev. 16 (2012) 599–617, <https://doi.org/10.1016/j.rser.2011.08.026>.
- [3] A. Makki, S. Omer, H. Sabir, Advancements in hybrid photovoltaic systems for enhanced solar cells performance, Renew. Sustain. Energy Rev. 41 (2015)

- 658–684.
- [4] T.T. Chow, G.N. Tiwari, C. Menezo, Hybrid solar: a review on photovoltaic and thermal power integration, *Int. J. Photoenergy* 2012 (2012).
  - [5] R.R. Avezov, J.S. Akhatov, N.R. Avezova, A review on photovoltaic-thermal (PV-T) air and water collectors, *Appl. Solar Energy* 47 (2011) 169–183.
  - [6] K.E. Amori, H.M.T. Al-Najjar, Analysis of thermal and electrical performance of a hybrid (PV/T) air based solar collector for Iraq, *Appl. Energy* 98 (2012) 384–395.
  - [7] A. Shahsavari, M. Ameri, Experimental investigation and modeling of a direct-coupled PV/T air collector, *Sol. Energy* 84 (2010) 1938–1958.
  - [8] J.J. Michael, S. Iniyar, R. Goic, Flat plate solar photovoltaic-thermal (PV/T) systems: A reference guide, *Renew. Sustain. Energy Rev.* 51 (2015) 62–88, <https://doi.org/10.1016/j.rser.2015.06.022>.
  - [9] A. Saxena, Varun, A.A. El-Sebaei, A thermodynamic review of solar air heaters, *Renew. Sustain. Energy Rev.* 43 (2015) 863–890, <https://doi.org/10.1016/j.rser.2014.11.059>.
  - [10] F. Hussain, M.Y.H. Othman, K. Sopian, B. Yatim, H. Ruslan, H. Othman, Design development and performance evaluation of photovoltaic/thermal (PV/T) air base solar collector, *Renew. Sustain. Energy Rev.* 25 (2013) 431–441, <https://doi.org/10.1016/j.rser.2013.04.014>.
  - [11] S. Singh, S. Agrawal, A. Tiwari, I.M. Al-Helal, D.V. Avasthi, Modeling and parameter optimization of hybrid single channel photovoltaic thermal module using genetic algorithms, *Sol. Energy* 113 (2015) 78–87, <https://doi.org/10.1016/j.solener.2014.12.031>.
  - [12] M.S. Thakare, G.S. Krishna Priya, P.C. Ghosh, S. Bandyopadhyay, Optimization of photovoltaic-thermal (PVT) based cogeneration system through water replenishment profile, *Sol. Energy* 133 (2016) 512–523, <https://doi.org/10.1016/j.solener.2016.04.037>.
  - [13] W. Fan, G. Kokogiannakis, Z. Ma, A multi-objective design optimisation strategy for hybrid photovoltaic thermal collector (PVT)-solar air heater (SAH) systems with fins, *Sol. Energy* 163 (2018) 315–328.
  - [14] Y.-Y. Hong, A.A. Beltran, A.C. Paglinawan, A robust design of maximum power point tracking using Taguchi method for stand-alone PV system, *Appl. Energy* 211 (2018) 50–63, <https://doi.org/10.1016/j.apenergy.2017.11.041>.
  - [15] A.N. Özakin, F. Kaya, Experimental thermodynamic analysis of air-based PVT system using fins in different materials: Optimization of control parameters by Taguchi method and ANOVA, *Sol. Energy* 197 (2020) 199–211, <https://doi.org/10.1016/j.solener.2019.12.077>.
  - [16] H.S. Hama, N. Kapur, Z. Khatir, O.M. Querin, H.M. Thompson, Y. Wang, M.C.T. Wilson, Computational fluid dynamics analysis and optimisation of polymerase chain reaction thermal flow systems, *Appl. Therm. Eng.* 183 (2021) 116122, <https://doi.org/10.1016/j.applthermaleng.2020.116122>.
  - [17] A.A. Hegazy, Comparative study of the performances of four photovoltaic/thermal solar air collectors, *Energy Convers. Manage.* 41 (2000) 861–881.
  - [18] J.A. Duffie, W.A. Beckman, *Solar engineering of thermal processes*, Wiley, New York, 1991.
  - [19] S. Youcef-Ali, Study and optimization of the thermal performances of the offset rectangular plate fin absorber plates, with various glazing, *Renew. Energy* 30 (2005) 271–280.
  - [20] S. Youcef-Ali, J.Y. Desmons, Numerical and experimental study of a solar equipped with offset rectangular plate fin absorber plate, *Renew. Energy* 31 (2006) 2063–2075.
  - [21] M. Al-Damook, Z.A.H. Obaid, M. Al Qubeissi, D. Dixon-Hardy, J. Cottom, P. J. Heggs, CFD modeling and performance evaluation of multipass solar air heaters, *Numer. Heat Transf. Part A: Appl.* 76 (2019) 438–464.
  - [22] O.K. Ahmed, Z.A. Mohammed, Dust effect on the performance of the hybrid PV/Thermal collector, *Therm. Sci. Eng. Prog.* 3 (2017) 114–122.
  - [23] O.K. Ahmed, Z.A. Mohammed, Influence of porous media on the performance of hybrid PV/Thermal collector, *Renew. Energy* 112 (2017) 378–387.
  - [24] T. Rajaseenivasan, S. Srinivasan, K. Srihar, Comprehensive study on solar air heater with circular and V-type turbulators attached on absorber plate, *Energy* 88 (2015) 863–873.
  - [25] K.E. Amori, M.A. Abd-AlRaheem, Field study of various air based photovoltaic/thermal hybrid solar collectors, *Renew. Energy* 63 (2014) 402–414.
  - [26] H.P. Garg, R.S. Adhikari, Conventional hybrid photovoltaic/thermal (PV/T) air heating collectors: steady-state simulation, *Renew. Energy* 11 (1997) 363–385.
  - [27] S.C. Solanki, S. Dubey, A. Tiwari, Indoor simulation and testing of photovoltaic thermal (PV/T) air collectors, *Appl. Energy* 86 (2009) 2421–2428.
  - [28] F.P. Incropera, A.S. Lavine, T.L. Bergman, D.P. DeWitt, *Fundamentals of heat and mass transfer*, Wiley, 2007.
  - [29] Y.A. Cengel, A. Ghajar, *Heat and mass transfer (a practical approach, SI version)*, McGraw-Hill Education, n.d., 2011.
  - [30] A.S. Joshi, A. Tiwari, G.N. Tiwari, I. Dincer, B.V. Reddy, Performance evaluation of a hybrid photovoltaic thermal (PV/T)(glass-to-glass) system, *Int. J. Therm. Sci.* 48 (2009) 154–164.
  - [31] J.C. Mojumder, W.T. Chong, H.C. Ong, K.Y. Leong, Abdullah-Al-Mamoon, An experimental investigation on performance analysis of air type photovoltaic thermal collector system integrated with cooling fins design, *Energy Build.* 130 (2016) 272–285, <https://doi.org/10.1016/j.enbuild.2016.08.040>.
  - [32] M.A.A. Al-Damook, Performance analysis of air-cooled photovoltaic/thermal systems, Ph.D., University of Leeds, 2019. <http://theses.whiterose.ac.uk/25298/> (accessed March 27, 2020).
  - [33] The European Commission's science and knowledge service, Photovoltaic Geographical Information System (PVGIS), (2020). <https://ec.europa.eu/jrc/en/pvgis>.
  - [34] R. Zorer, C.G. Volschenk, J.J. Hunter, Integrating Geographic Information Systems and hemispherical photography in the assessment of canopy light profiles in a vineyard, *Agric. For. Meteorol.* 232 (2017) 672–681.
  - [35] A. Bocca, L. Bottaccioli, E. Chiavazza, M. Fasano, A. Macii, P. Asinari, Estimating photovoltaic energy potential from a minimal set of randomly sampled data, *Renew. Energy* 97 (2016) 457–467.
  - [36] D. Palmer, I. Cole, T. Betts, R. Gottschalg, Interpolating and estimating horizontal diffuse solar irradiation to provide UK-wide coverage: Selection of the best performing models, *Energies* 10 (2017) 181.
  - [37] M. Khaki, A. Shahsavari, S. Khanmohammadi, M. Salmazadeh, Energy and exergy analysis and multi-objective optimization of an air based building integrated photovoltaic/thermal (BIPV/T) system, *Sol. Energy* 158 (2017) 380–395.
  - [38] M. Ahmed-Dahmane, A. Malek, T. Zitoun, Design and analysis of a BIPV/T system with two applications controlled by an air handling unit, *Energy Convers. Manage.* 175 (2018) 49–66.
  - [39] A. Handbook, Heating, ventilating, and air-conditioning applications, ASHRAE, Atlanta (GA), 2007).
  - [40] A. Shahsavari, S. Khanmohammadi, Feasibility of a hybrid BIPV/T and thermal wheel system for exhaust air heat recovery: Energy and exergy assessment and multi-objective optimization, *Appl. Therm. Eng.* 146 (2019) 104–122.
  - [41] M. Mattei, G. Notton, C. Cristofari, M. Muselli, P. Poggi, Calculation of the polycrystalline PV module temperature using a simple method of energy balance, *Renew. Energy* 31 (2006) 553–567, <https://doi.org/10.1016/j.renene.2005.03.010>.
  - [42] J.A. del Cueto, Comparison of energy production and performance from flat-plate photovoltaic module technologies deployed at fixed tilt, in: Conference Record of the Twenty-Ninth IEEE Photovoltaic Specialists Conference, 2002, 2002, pp. 1523–1526. <https://doi.org/10.1109/PVSC.2002.1190901>.
  - [43] H.-U. Bernard, R.D. Burk, Z. Chen, K. van Doorslaer, H. zur Hausen, E.-M. de Villiers, Classification of papillomaviruses (PVs) based on 189 PV types and proposal of taxonomic amendments, *Virology*. 401 (2010) 70–79. <https://doi.org/10.1016/j.virol.2010.02.002>.
  - [44] M.A. Green, K. Emery, Y. Hishikawa, W. Warta, E.D. Dunlop, Solar cell efficiency tables (Version 45), *Prog. Photovoltaics Res. Appl.* 23 (2015) 1–9, <https://doi.org/10.1002/ppp.2573>.
  - [45] Hamakawa Y. Ed. Thin-film solar cells: next generation photovoltaics and its applications Springer Berlin ; New York ISBN 978-3-540-43945-5 2004
  - [46] C.S. Rajoria, P.K. Gupta, S. Agrawal, G.N. Tiwari, D. Singh, Effect of Different Photovoltaic Materials on Energetic and Exergetic Performance of Photovoltaic Thermal Arrays, in: MATEC Web of Conferences, EDP Sciences, 2017, p. 01006.
  - [47] P. Dupeyrat, C. Ménézo, M. Rommel, H.-M. Henning, Efficient single glazed flat plate photovoltaic-thermal hybrid collector for domestic hot water system, *Sol. Energy* 85 (2011) 1457–1468.
  - [48] Advances in crystalline silicon solar cell technology for industrial mass production | NPG Asia Materials, (n.d.). <https://www.nature.com/articles/am201082> (accessed March 27, 2020).
  - [49] M. Al-Damook, D. Dixon-Hardy, P.J. Heggs, M. Al Qubeissi, K. Al-Ghathithi, P.E. Mason, J. Cottom, CFD analysis of a one-pass photovoltaic/thermal air system with and without offset strip fins, in: MATEC Web of Conferences, EDP Sciences, 2018, p. 03002.
  - [50] Friction Factor for Laminar Flow, Nuclear Power. (n.d.). <https://www.nuclear-power.net/nuclear-engineering/fluid-dynamics/major-head-loss-friction-loss/friction-factor-for-laminar-flow/> (accessed March 25, 2020).
  - [51] Z.T. Ai, C.M. Mak, Pressure losses across multiple fittings in ventilation ducts, *Sci. World J.* 2013 (2013).
  - [52] R.L. Daugherty, Fluid mechanics with engineering applications, Tata McGraw-Hill Education, 1989.
  - [53] D.F. Young, B.R. Munson, T.H. Okiishi, W.W. Huebsch, A brief introduction to fluid mechanics, John Wiley & Sons, 2010.
  - [54] S. Rai, P. Chand, S.P. Sharma, Evaluation of thermo hydraulic effect on offset finned absorber solar air heater, *Renew. Energy* 125 (2018) 39–54.
  - [55] S. Rai, P. Chand, S.P. Sharma, An analytical investigations on thermal and thermohydraulic performance of offset finned absorber solar air heater, *Sol. Energy* 153 (2017) 25–40.
  - [56] M.K. Mittal, L. Varshney, Optimal thermohydraulic performance of a wire mesh packed solar air heater, *Sol. Energy* 80 (2006) 1112–1120.
  - [57] A. Cortes, R. Piacentini, Improvement of the efficiency of a bare solar collector by means of turbulence promoters, *Appl. Energy* 36 (1990) 253–261.
  - [58] I.-R. Caluianu, F. Băltărețu, Thermal modelling of a photovoltaic module under variable free convection conditions, *Appl. Therm. Eng.* 33 (2012) 86–91.
  - [59] M.U. Siddiqui, A.F. Arif, L. Kelley, S. Dubowsky, Three-dimensional thermal modeling of a photovoltaic module under varying conditions, *Sol. Energy* 86 (2012) 2620–2631.
  - [60] K. Kant, A. Shukla, A. Sharma, P.H. Biwole, Thermal response of polycrystalline silicon photovoltaic panels: Numerical simulation and experimental study, *Sol. Energy* 134 (2016) 147–155.
  - [61] S. Dubey, J.N. Sarvaiya, B. Seshadri, Temperature dependent photovoltaic (PV) efficiency and its effect on PV production in the world-a review, *Energy Procedia* 33 (2013) 311–321.

- [62] N. Aste, C. del Pero, F. Leonforte, Water flat plate PV-thermal collectors: a review, *Sol. Energy* 102 (2014) 98–115.
- [63] D.L. Evans, Simplified method for predicting photovoltaic array output, *Sol. Energy* 27 (1981) 555–560.
- [64] G. Nottton, C. Cristofari, M. Mattei, P. Poggi, Modelling of a double-glass photovoltaic module using finite differences, *Appl. Therm. Eng.* 25 (2005) 2854–2877.
- [65] F. Sarhaddi, S. Farahat, H. Ajam, A. Behzadmehr, M.M. Adeli, An improved thermal and electrical model for a solar photovoltaic thermal (PV/T) air collector, *Appl. Energy* 87 (2010) 2328–2339.
- [66] W. Fan, G. Kokogiannakis, Z. Ma, P. Cooper, Development of a dynamic model for a hybrid photovoltaic thermal collector–Solar air heater with fins, *Renew. Energy* 101 (2017) 816–834.
- [67] M. Al Hamdani, M. Al Qubeissi, M. Al-Damook, D. Dixon-Hardy, P. Heggs, Thermal Optimisation of Fin Clusters for Heat Sink Purposes, in: ICTEA: International Conference on Thermal Engineering, 2018.
- [68] K.G.T. Hollands, E.C. Shewen, Optimization of flow passage geometry for air-heating, plate-type solar collectors, 1981.
- [69] I. Tosun, D. Uner, C. Ozgen, Critical Reynolds number for Newtonian flow in rectangular ducts, *Ind. Eng. Chem. Res.* 27 (10) (1988) 1955–1957 <https://doi.org/10.1021/ie00082a034>.
- [70] F. Durst, S. Ray, B. Ünsal, O.A. Bayoumi, The development lengths of laminar pipe and channel flows, 2005.
- [71] A. Narayanan, V.V. Toropov, A.S. Wood, I.F. Campean, Simultaneous model building and validation with uniform designs of experiments, *Eng. Optim.* 39 (2007) 497–512, <https://doi.org/10.1080/03052150701399978>.
- [72] A.F. Al-Neama, Z. Khatir, N. Kapur, J. Summers, H.M. Thompson, An experimental and numerical investigation of chevron fin structures in serpentine minichannel heat sinks, *Int. J. Heat Mass Transf.* 120 (2018) 1213–1228, <https://doi.org/10.1016/j.ijheatmasstransfer.2017.12.092>.
- [73] Z. Khatir, A.R. Taherkhani, J. Paton, H. Thompson, N. Kapur, V. Toropov, Energy thermal management in commercial bread-baking using a multi-objective optimisation framework, *Appl. Therm. Eng.* 80 (2015) 141–149, <https://doi.org/10.1016/j.applthermaleng.2015.01.042>.
- [74] S.A. Sarra, Regularized symmetric positive definite matrix factorizations for linear systems arising from RBF interpolation and differentiation, *Eng. Anal. Boundary Elem.* 44 (2014) 76–86, <https://doi.org/10.1016/j.enganabound.2014.04.019>.
- [75] Z. Khatir, K.J. Kubiak, P.K. Jimaek, T.G. Mathia, Dropwise condensation heat transfer process optimisation on superhydrophobic surfaces using a multi-disciplinary approach, *Appl. Therm. Eng.* 106 (2016) 1337–1344, <https://doi.org/10.1016/j.applthermaleng.2016.06.128>.
- [76] Z. Khatir, A.D. Lucey, A combined boundary integral and vortex method for the numerical study of three-dimensional fluid flow systems, *Int. J. Comput. Math.* 89 (2012) 1504–1524, <https://doi.org/10.1080/00207160.2012.695354>.
- [77] C.M. Fonseca, P.J. Fleming, *Genetic Algorithms for Multiobjective Optimization: Formulation Discussion and Generalization*, ICGA, Citeseer (1993) 416–423.
- [78] K. Deb, S. Agrawal, A. Pratap, T. Meyarivan, A. Fast, Elitist Non-dominated Sorting Genetic Algorithm for Multi-objective Optimization: NSGA-II, in: M. Schoenauer, K. Deb, G. Rudolph, X. Yao, E. Lutton, J.J. Merelo, H.-P. Schwefel (Eds.), *Parallel Problem Solving from Nature PPSN VI*, Springer, Berlin, Heidelberg, 2000, pp. 849–858, [https://doi.org/10.1007/3-540-45356-3\\_83](https://doi.org/10.1007/3-540-45356-3_83).
- [79] M.M. Adeli, F. Sobhnamayan, S. Farahat, M.A. Alavi, F. Sarhaddi, Experimental performance evaluation of a photovoltaic thermal (PV/T) air collector and its optimization, *Strojnikski Vestnik-J. Mech. Eng.* 58 (2012) 309–318.
- [80] A.A. Farhan, M. Alaskari, A. Alhamdani, A parametric study of a photovoltaic panel with cylindrical fins under still and moving air conditions in Iraq, *Heat Transf.* (2020).